



Die Grenzen der
Chemie neu ausloten?
It takes
#HumanChemistry

Wir suchen kreative Chemikerinnen und Chemiker,
die mit uns gemeinsam neue Wege gehen wollen –
mit Fachwissen, Unternehmertum und Kreativität für
innovative Lösungen. Informieren Sie sich unter:

[evonik.de/karriere](https://www.evonik.de/karriere)

Simulation of Hot Isostatic Pressing in a Single-Crystal Ni Base Superalloy with the Theory of Continuously Distributed Dislocations Combined with Vacancy Diffusion

Titus Feldmann, Bernard Fedelich,* and Alexander Epishin

Single-crystal components made of nickel base superalloys contain pores after casting and homogenization heat treatment. Hot isostatic pressing (HIP), which is carried above the γ' -solvus temperature of the alloy, is industrially applied to reduce porosity. A modeling of HIP based on continuously distributed dislocations is developed in a 2D setting. Glide and climb of straight-edge dislocations, as well as vacancy diffusion, are the deformation mechanisms taken into account. Thereby, dislocation glide is controlled by dragging a cloud of large atoms, and climb is controlled by vacancy diffusion. Relying on previous investigations of the creep behavior at HIP temperatures, it is assumed that new dislocations are nucleated at low-angle boundaries (LAB) and move through subgrains until they either reach the opposite LABs or react with other dislocations and annihilate. Vacancies are created at the pore surface and diffuse through the alloy until they are either consumed by climbing dislocations or disappear at the LABs. The field equations are solved by finite elements. It is shown that pore shrinking is mostly controlled by vacancy diffusion as the shear stresses at the LABs are too low to nucleate a sufficient amount of dislocations.

50 μm form during solidification (S-pores, see Figure 1a) and small round pores of size up to 10 μm form during the homogenization heat treatment (H-pores, see Figure 1b). It has been shown (see, e.g., the study by Epishin^[4]) that pores are detrimental to the fatigue strength of the alloys as they favor crack initiation. Hence, hot isostatic pressing (HIP) is widely performed to reduce the porosity. However, HIP is a costly process that can only be performed in a narrow-parameter window and bears the risk of altering the microstructure by recrystallization and incipient melting. For example, HIP of the widely used single-crystal superalloy CMSX-4^[5] is carried out at 1288 °C in an argon chamber under the pressure of 103 MPa. At this temperature, the strengthening γ' precipitates are almost completely dissolved and the material is very soft. In consequence, efforts have been made in

1. Introduction

Single crystals of nickel-base superalloys are commonly used as blade material in the hottest sections of gas turbines or aero engines. After casting and heat treatment, the components contain pores of various sizes^[1–3]. Large irregular pores of size up to

the recent past to better understand the mechanisms of pore closure during HIP and develop numerical models of pore shrinking under HIP that would allow for process optimization.^[3,6–8]


A preliminary condition for the development of such models is that the clarification of the physical mechanisms of porosity decrease. In turn, this question can only be answered if the dominant deformation mechanisms under HIP conditions are identified. In principle, two mechanisms can be expected: dislocation creep and vacancy diffusion creep. In a series of short-term (<10 h) creep tests, the deformation behavior of the alloy CMSX-4 at 1288 °C,^[9] and of a γ -phase alloy with a similar composition to CMSX-4 in a broader temperature range,^[10] were investigated. The results can be summarized as follows: (111)(011) octahedral glide is the dominant deformation mechanism at 1288 °C for short-term creep. The orientation dependence of the creep strength is high and agrees with octahedral glide. Also, the creep exponent lies between 5 and 6 and is fully consistent with the dominance of dislocation creep. In both alloys, the characteristic microstructure at 1288 °C consists of subgrains separated by low-angle boundaries (LAB). Dislocations were hardly observed within the subgrains. It was conjectured in the study by Epishin et al.^[10] that dislocations are nucleated at the LABs, glide across the subgrains, and finally reach the opposite LABs where they rearrange to maintain a low-energy dislocation structure.

T. Feldmann, B. Fedelich

Experimental and Model Based Mechanical Behaviour of Materials
Bundesanstalt für Materialforschung und -prüfung (BAM) Division 5.2
Experimentelle und modellbasierte Werkstoffmechanik
Unter den Eichen 87, 12205 Berlin, Germany
E-mail: bernard.fedelich@bam.de

A. Epishin

Department of shock-wave processes Merzhanov Institute of Structural
Macrokineics and Materials Science
Russian Academy of Sciences
Academician Osipyan St. 8, Chernogolovka, Moscow Region 142432,
Russia

 The ORCID identification number(s) for the author(s) of this article can be found under <https://doi.org/10.1002/adem.202101341>.

© 2021 The Authors. Advanced Engineering Materials published by Wiley-VCH GmbH. This is an open access article under the terms of the Creative Commons Attribution License, which permits use, distribution and reproduction in any medium, provided the original work is properly cited.

DOI: 10.1002/adem.202101341

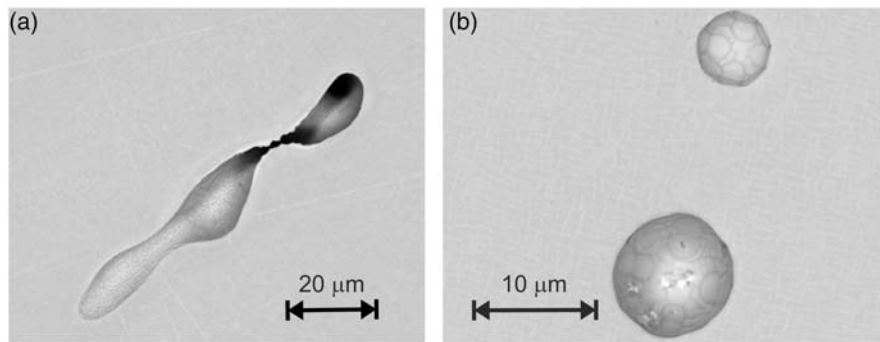


Figure 1. Scanning electron microscope views of a) S-pores and b) H-pores.

Consistent with the observed dominance of octahedral glide, crystal plasticity (CP) was applied to simulate pore shrinking.^[6,7] The first simulations^[6] assumed gas-free pores and largely overestimated the rate of pore shrinking. This is also true for the more recent simulations^[7] at the beginning of HIP (<1 h). In addition, the plasticity localizes at corners and the pores readily lost their initial spherical symmetry, which is not the case in experiments.^[11] Considering the case of additively manufactured (AM) parts, Prasad et al.^[7] assumed that argon gas, which is present in the AM build chamber, remains trapped in the pores. When the pores shrink, the gas pressure increases and increasingly opposes further pore shrinking, hence significantly reducing the porosity reduction rate. However, it is not clear whether gas also remains trapped in the pores of cast alloys. Indeed, the solidification of single-crystal turbine blades is a vacuum technology and the amount of gas inside the pores should be limited. In addition, following the study by Levinsky,^[12] it should be expected that the gas trapped in the voids partly dissolves at the pore/metal interface according to Sievert's law when its partial pressure increases. Hence, simulations assuming a constant gas amount in the pores necessarily underestimate the porosity decrease rate.

In parallel, simulations of pore shrinking based on the mechanism of vacancy diffusion creep were developed in other studies.^[3,11] More specifically, the stationary vacancy diffusion equation was solved in a hollow sphere containing a spherical pore, the exterior surface representing a LAB. The calculations assumed that vacancies form at the pore surface and diffuse to the LAB where they are annihilated. Taking into account measurements of the initial pore size distribution, a remarkable agreement with the porosity decrease detected by synchrotron tomography was reported in the study by Epishin et al.^[3] In addition, the remaining porosity observed by scanning electron microscopy (SEM) after 0.5 h of HIP was reasonably well predicted in a pressure range between 15 and 100 MPa. A higher deviation was observed for a pressure of 150 MPa, for which the porosity decrease was underestimated. The good agreement of the estimates of porosity decrease by the diffusion model and its overestimation by the crystal viscoplasticity models provide a strong argument for the dominance of vacancy diffusion during pore shrinking.

However, as octahedral glide was shown to be the dominant deformation mechanism under HIP conditions, the question arises as to why vacancy diffusion appears to control porosity reduction during HIP. As a matter of fact, the applicability of classical viscoplasticity at the porosity scale (<100 μm) is

questionable, as it implicitly assumes that perfect dislocation sources are everywhere available. However, as mentioned earlier, it is likely that under HIP conditions, the dislocations are emitted at the LABs and move across the subgrains before they reach the next LABs. Hence, a model that extends classical viscoplasticity to dislocation nucleation at LABs and transports through the subgrains is desirable to resolve this contradiction.

In accordance with the previous considerations, this article presents the development of a continuum dislocation/vacancy model at the scale of the subgrains (also called dislocation cells or mosaic blocks in the study by Bruckner et al.^[13]) to simulate pore shrinking during the HIP process. These subgrains, which are separated by LABs, correspond to substructures of the dendrites. They have a misorientation lower than 0.5° while the misorientations between the dendrites can be as high as 2°–3°.^[13] Hence, at this level, it is not realistic to assume a uniform distribution of dislocation sources as usual in CP. While climb was shown in the study by Epishin et al.^[9] to play a minor role for uniaxial creep, it could influence the process of pore shrinking due to the complex stress state around a pore. Hence, the porosity reduction model should take into account: 1) dislocation transport away from the sources, which are assumed to be located at the LABs, 2) pore shrinking due to vacancy diffusion and dislocation creep, 3) dislocation glide and climb, 4) dipole annihilation by climb, and 5) back-stresses due to short-range interactions between dislocations.

To simplify, a 2D model is considered, consisting of a disk bounded by LABs containing a circular pore and in which straight-edge dislocations move on three different slip systems. The model has been formulated in the small strains/small rotations framework. Hence, it is not appropriate to simulate full pore shrinking but rather to identify the relative magnitudes of the two main pore closure mechanisms: vacancy diffusion and dislocation creep. Due to these restrictions, the present simulations have a qualitative character. It should be also mentioned that an extension to 3D would dramatically increase the complexity of the model due to the much larger number of unknowns and the necessity to account for the balance of curved dislocations.^[14]

This article is organized as follows. First, in Section 2, the notations are introduced and the field equations resulting from the balance equations as well as the kinematics of glide and climb in a 2D crystal are summarized. At the scale considered here, it is expected that short-range interactions between dislocations (usually called back-stresses in constitutive modeling) play a role.

An energy-based extension of the back-stress derived by Groma^[13] to include multiple slip systems and climb is proposed in Section 3. Dislocation mobility is assumed to be controlled by dragging of large solute atoms around the core by diffusion (Cottrell atmosphere). The calculation of the corresponding drag coefficient for glide and climb is developed in Section 4. In agreement with the available transmission electron microscopy (TEM) observations,^[9,10] it is assumed that the interior of the subgrains is initially free from dislocations. Instead, it is assumed that dislocations are emitted at the LABs. The intensity of the dislocation sources has been identified by comparison with the creep rates measured with the single-crystal superalloy CMSX-4 at 1288 °C in Section 5. Finally, simulations of pore shrinking with the theory developed in this work are presented in Section 6. The model parameters have been chosen for the alloy CMSX-4, as described in Appendix 1. The influence of pore size and position, elastic anisotropy, as well as the magnitude of the vacancy diffusion coefficient are investigated.

2. Presentation of the Field Equations and Model Variables

This section introduces the notations used in this article, the most important assumptions and simplifications, the relevant balance equations, and summarizes the kinematic relations for dislocation glide and climb. As already mentioned earlier, the present theory has been developed in a 2D setting. In accordance, straight-edge dislocations parallel to the z axis move in the (x,y) plane. A distinction is made between the dislocation level (microscopic scale) with a singular displacement field $\tilde{\mathbf{u}}(\mathbf{x}, t)$ and the continuum level (mesoscopic scale) with a smooth displacement field $\mathbf{u}(\mathbf{x}, t)$.

2.1. Kinematics of CP with Dislocation Climb

In the following sections, the basic notations for dislocations loops in 3D and the derivation of the 2D kinematics from 3D rectangular dislocations are summarized for definiteness. The unit line vector along the dislocation is ξ and the normal vector to ξ in the glide plane is denoted by ζ (see Figure 2). In accordance with the convention used in the study by Hirth et al.,^[16] the Burgers vector is defined as an integral along a closed-circuit \mathcal{C} around the dislocation loop \mathcal{L} taken in the right-handed sense relative to ξ

$$\mathbf{b} = \oint_{\mathcal{C}} \frac{\partial \tilde{\mathbf{u}}}{\partial l} dl = \tilde{\mathbf{u}}^- - \tilde{\mathbf{u}}^+ = -\tilde{\mathbf{u}} \quad (1)$$

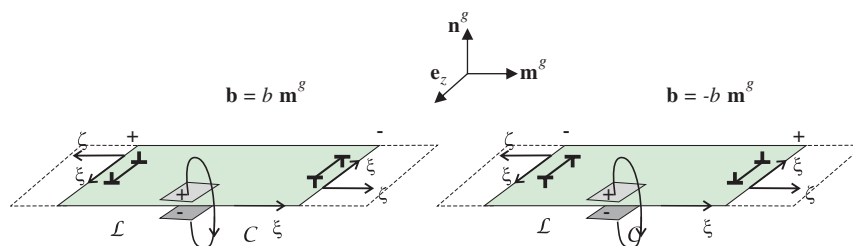


Figure 2. Geometry of dislocation loops with $\mathbf{b} = b \mathbf{m}^g$ and $\mathbf{b} = -b \mathbf{m}^g$.

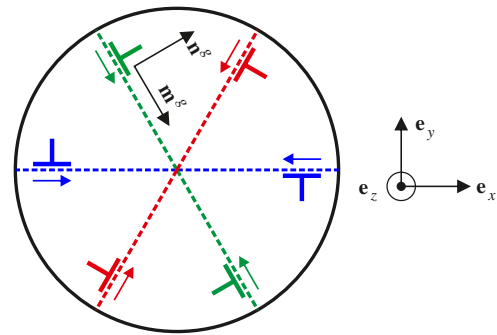


Figure 3. The three-slip systems and six dislocation types of the 2D model.

and corresponds to the opposite of the jump $\tilde{\mathbf{u}}$ of the displacement across the surface cut by the dislocation.

We consider an arrangement of three glide systems $g = 1, 2, 3$, making an angle of 60° , with unit normal vector \mathbf{n}^g and unit glide vector \mathbf{m}^g , such that $(\mathbf{m}^g, \mathbf{n}^g, \mathbf{e}_z)$ is right handed (see Figure 3). Each slip system includes two dislocation types denoted by the superscript s ($s = +, -$), depending on the location of the additional atomic half plane with respect to the glide plane. In a 3D picture, these dislocations can be envisioned as the long segments of rectangular closed loops, as shown in Figure 2. Because $+\mathbf{b}$ and $-\mathbf{b}$ are possible Burgers vectors for any glide system, two dislocation types, $+$ and $-$, are possible, respectively whenever $\mathbf{b} \cdot \zeta < 0$ and $\mathbf{b} \cdot \zeta > 0$ (see Figure 2), which provides the connection to the 2D description. In total, six types of dislocations (g, s) are considered.

At the continuum level, the average distortion rate $\dot{\beta}^{\text{in}}$ caused by N dislocations of length L denoted by the superscript I , with the Burgers vector \mathbf{b}^I , and moving with their respective velocities $\tilde{\mathbf{v}}^I$ in the volume \mathcal{V} is

$$\dot{\beta}^{\text{in}} = \frac{NL}{\mathcal{V}} \sum_I \mathbf{b}^I \otimes (\xi^I \times \tilde{\mathbf{v}}^I) \quad (2)$$

Note that the inelastic distortion is related to the inelastic strain ϵ^{in} by $\epsilon^{\text{in}} = \frac{1}{2} (\dot{\beta}^{\text{in}} + (\dot{\beta}^{\text{in}})^T)$. The total dislocation number N can be decomposed in the contributions N^{gs} for each dislocation type (g, s). The corresponding dislocation densities are introduced as $\rho^{gs} = N^{gs} L / \mathcal{V}$ and the average dislocation velocities at the slip system level are denoted by \mathbf{v}^{gs} . The overall dislocation density of the slip system g is $\rho^g = \rho^{g+} + \rho^{g-}$ and the density of geometrically necessary dislocations (GNDs) for the system g is $\kappa^g = \rho^{g+} - \rho^{g-}$. The velocity \mathbf{v}^{gs} is decomposed in a glide and a climb component according to

$$\mathbf{v}^{gs} = v_{gl}^{gs} \mathbf{m}^g + v_{cl}^{gs} \mathbf{n}^g, \quad s = +, - \quad (3)$$

After some rearrangements, the resulting inelastic distortion rate is

$$\begin{aligned} \dot{\boldsymbol{\beta}}^{\text{in}} = & b \sum_g (\rho^{g+} v_{gl}^{g+} - \rho^{g-} v_{gl}^{g-}) \mathbf{m}^g \otimes \mathbf{n}^g \\ & + (-\rho^{g+} v_{cl}^{g+} + \rho^{g-} v_{cl}^{g-}) \mathbf{m}^g \otimes \mathbf{m}^g \end{aligned} \quad (4)$$

In the case of pure glide, and assuming symmetry, that is, $v_{gl}^{g+} = -v_{gl}^{g-} = v_{gl}^g$, Equation (4) becomes

$$\dot{\boldsymbol{\beta}}^{\text{in}} = \sum_g \dot{\gamma}^g \mathbf{m}^g \otimes \mathbf{n}^g \quad (5)$$

and one recovers the usual Orowan equation with

$$\dot{\gamma}^g = b(\rho^{g+} v_{gl}^{g+} - \rho^{g-} v_{gl}^{g-}) = b(\rho^{g+} v_{gl}^g + \rho^{g-} v_{gl}^g) = b \rho^g v_{gl}^g \quad (6)$$

The volumic part of the inelastic distortion rate (4) is

$$\text{tr}(\dot{\boldsymbol{\beta}}^{\text{in}}) = \text{tr}(\dot{\boldsymbol{\epsilon}}^{\text{in}}) = b \sum_g (-\rho^{g+} v_{cl}^{g+} + \rho^{g-} v_{cl}^{g-}) \quad (7)$$

If $\boldsymbol{\sigma}$ denotes the stress tensor at the continuum level, the resolved shear stress (RSS) for the system g is introduced as

$$\tau^g = \mathbf{n}^g \cdot \boldsymbol{\sigma} \cdot \mathbf{m}^g \quad (8)$$

and the stress component responsible for climb is

$$\zeta^g = \mathbf{m}^g \cdot \boldsymbol{\sigma} \cdot \mathbf{m}^g \quad (9)$$

With these last definitions, the inelastic power immediately results from the inelastic distortion rate (4) as

$$\begin{aligned} \boldsymbol{\sigma} : \dot{\boldsymbol{\beta}}^{\text{in}} = & b \sum_g \tau^g (\rho^{g+} v_{gl}^{g+} - \rho^{g-} v_{gl}^{g-}) + \zeta^g (-\rho^{g+} v_{cl}^{g+} + \rho^{g-} v_{cl}^{g-}) \\ = & b \sum_{g,s} \tau^{gs} \rho^{gs} v_{gl}^{gs} + \zeta^{gs} \rho^{gs} v_{cl}^{gs} \end{aligned} \quad (10)$$

in which the glide and climb stress components for each dislocation family (g, s) are

$$\tau^{gs} = \begin{cases} \tau^g & \text{if } s = + \\ -\tau^g & \text{if } s = - \end{cases}, \quad \zeta^{gs} = \begin{cases} -\zeta^g & \text{if } s = + \\ \zeta^g & \text{if } s = - \end{cases} \quad (11)$$

The dislocation density tensor $\boldsymbol{\alpha}$ provides the resulting Burgers vector $d\mathbf{b}$ of the dislocations piercing a surface element dS of normal vector \mathbf{n} through the relationship $d\mathbf{b} = \boldsymbol{\alpha} \cdot \mathbf{n} dS$ (see, for example, the study by Mura^[17]), and is given in the present case by

$$\boldsymbol{\alpha} = \frac{NL}{V} \sum_I \mathbf{b}^I \otimes \boldsymbol{\xi}^I \quad (12)$$

As mentioned earlier (see also Figure 2), for each slip system g , the Burgers vectors $\mathbf{b}^I = b \mathbf{m}^g$, $\mathbf{b}^I = -b \mathbf{m}^g$ and the line vectors $\boldsymbol{\xi}^I = \mathbf{e}_z$, $\boldsymbol{\xi}^I = -\mathbf{e}_z$, are possible. In accordance, the dislocation segments I can be rearranged into three slip systems $g = 1, 2, 3$

and, respectively, two dislocation types $(+, -)$. Hence, Equation (12) can be rewritten

$$\begin{aligned} \boldsymbol{\alpha} = & \frac{L}{V} b \sum_{g=1}^3 (N^{g+} - N^{g-}) \mathbf{m}^g \otimes \mathbf{e}_z \\ = & b \sum_{g=1}^3 (\rho^{g+} - \rho^{g-}) \mathbf{m}^g \otimes \mathbf{e}_z = b \sum_{g=1}^3 \kappa^g \mathbf{m}^g \otimes \mathbf{e}_z \end{aligned} \quad (13)$$

Note that the dislocation density tensor is also related to the elastic and inelastic distortions (see, for example, the study by Teodosiu^[18]) by

$$\boldsymbol{\alpha} = \nabla \times \boldsymbol{\beta}^{\text{el}} = -\nabla \times \boldsymbol{\beta}^{\text{in}} \quad (14)$$

or in index notation $\alpha_{ij} = \epsilon_{jkl} \beta_{il,k}^{\text{el}}$, in which ϵ_{jkl} is a component of the permutation tensor (Levi–Civita symbol).

2.2. The Peach–Köhler Force on Gliding and Climbing Dislocations

The Peach–Köhler force is the mechanical force exerted by the microscopic scale stress field $^* \tilde{\boldsymbol{\sigma}}$ on individual dislocations (see, e.g., the textbook by Hirth and Lothe^[16]). With the notations of Figure 2, the force acting on a dislocation segment reads

$$\tilde{\mathbf{F}}^{\text{PK}} = \mathbf{b} \cdot \tilde{\boldsymbol{\sigma}} \times \boldsymbol{\xi} \quad (15)$$

The glide component $\tilde{F}_{gl}^{\text{PK},g} = \tilde{\mathbf{F}}^{\text{PK}} \cdot \mathbf{m}^g$ and the climb component $\tilde{F}_{cl}^{\text{PK},g} = \tilde{\mathbf{F}}^{\text{PK}} \cdot \mathbf{n}^g$ are found to be $\tilde{F}_{gl}^{\text{PK},g+} = b \tilde{\tau}^g$, $\tilde{F}_{gl}^{\text{PK},g-} = -b \tilde{\tau}^g$, respectively, $\tilde{F}_{cl}^{\text{PK},g+} = -b \tilde{\zeta}^g$, $\tilde{F}_{cl}^{\text{PK},g-} = b \tilde{\zeta}^g$, which are the microscopic counterparts of Equation (11) at the continuum level.

2.3. Balance of Dislocation Density

The evolution of the dislocation density (g, s) is governed by the balance equation

$$\dot{\rho}^{gs} + \nabla \cdot (\rho^{gs} \mathbf{v}^{gs}) = p^{gs} - \omega^{gs} \quad (16)$$

where p^{gs} is a production and ω^{gs} a sink term. Equation (16) corresponds to the local form of a balance equation that applies for any conserved quantity in continuum physics (see, e.g., the textbook by Gurtin et al.^[19]). It has been also derived in the more general case (without sources or sinks) of curved dislocations by Mura (see, e.g., the textbook by Mura^[17]). In the following paragraphs, it will be assumed that dislocations are nucleated in the LABs only and thus $p^{gs} \equiv 0$. Hence,^[20] dislocation annihilation is due to gliding dislocations that meet a dislocation with the opposite Burgers vector lying on a slip plane of vertical distance lower than the critical distance

$$d_{\text{crit}}^g = \frac{\mu b}{8\pi(1-\nu)|\tau^g|} \quad (17)$$

Assuming symmetry between the systems $+$ and $-$, that is, $v_{gl}^{g+} = -v_{gl}^{g-} = v_{gl}^g$, the probability p^{g+} that a $+$ dislocation reacts

with a – dislocation during dt is the probability to find a – dislocation in a window of size $2|v_{gl}^g|dt \times 2d_{crit}^g$, that is, $p^{g+} = 4|v_{gl}^g|d_{crit}^g\rho^{g-}dt$. Hence, the sink term in Equation (16) is

$$\omega^{gs} = \omega^{g+} = \omega^{g-} = 4|v_{gl}^g|d_{crit}^g\rho^{g+}\rho^{g-} \quad (18)$$

Note that the difference of Equation (16) for + and – yields the balance equation for the GNDs.

$$\dot{\kappa}^g + \nabla \cdot (\rho^{g+}v^{g+} - \rho^{g-}v^{g-}) = \dot{\kappa}^g + \nabla \cdot (J_d^{g+} - J_d^{g-}) = 0 \quad (19)$$

where the dislocation flux for the type (g, s) is denoted $J_d^{gs} = \rho^{gs}v^{gs}$. Let \mathbf{n} denote the outer normal vector of the LAB that delimits the modeled region. The boundary conditions depend on the direction of the local dislocation velocity as follows. 1) If $v^{gs} \cdot \mathbf{n} < 0$, the LAB generates dislocations of the type (g, s) , as described in Section 5. 2) If $v^{gs} \cdot \mathbf{n} \geq 0$, the dislocations move toward the LAB and are annihilated by reaction with dislocations approaching the LAB from the opposite side, without altering the dislocation content of the LAB.

At a free surface (like the pore surface), no dislocations are nucleated if $v^{gs} \cdot \mathbf{n} < 0$. If $v^{gs} \cdot \mathbf{n} \geq 0$ the dislocations leave the simulated region.

2.4. Diffusion of Vacancies

Let $c_v(\mathbf{x}, t)$ denote the atomic vacancy concentration ($0 \leq c_v \leq 1$). The connection between vacancy conservation and climb deformation at the continuum scale has been analyzed in the study by Geers et al.^[21] If \mathbf{J}_v denotes the vacancy flux, the vacancies' balance equation is

$$\dot{c}_v = -\nabla \cdot \mathbf{J}_v + tr(\dot{\epsilon}^{in}) \quad (20)$$

where $tr(\dot{\epsilon}^{in})$ is given by Equation (7). The vacancy flux is proportional to the gradient of the diffusion potential μ_v

$$\mathbf{J}_v = -M_v \nabla \mu_v \quad (21)$$

where the mobility coefficient is given by $M_v = \frac{D_v \Omega}{kT} c_v (1 - c_v)$ and the diffusion potential by (see the study by Gao et al.^[22])

$$\mu_v = \frac{kT}{\Omega} \left(\ln \frac{c_v}{1 - c_v} + \frac{Q_v}{kT} - \frac{1}{3} \frac{tr \sigma \Delta V_r}{kT} \right) \quad (22)$$

The diffusion potential Equation (22) depends on the vacancy formation energy Q_v and $-\frac{1}{3}tr \sigma \Delta V_r$, which is the energy release when an atom is removed. Inserting the flux (21) into Equation (20) and taking into account (22) with the simplifications $c_v \ll 1$ and $\frac{1}{3}|tr \sigma \Delta V_r| \ll Q_v$ yields

$$\dot{c}_v = D_v \Delta c_v + tr(\dot{\epsilon}^{in}) \quad (23)$$

Let us denote by c_{v0} the equilibrium concentration of vacancies at the considered temperature, that is

$$c_{v0} = \exp\left(-\frac{Q_v}{kT}\right) \quad (24)$$

At the external boundary ∂V of the solid V , the diffusion potential is given by $\mu_v = \mathbf{n} \cdot \boldsymbol{\sigma} \cdot \mathbf{n}$, which leads under the simplifications mentioned above to the following Dirichlet boundary condition (BC)

$$c_v = c_{v0} \exp\left(\frac{\Omega \mathbf{n} \cdot \boldsymbol{\sigma} \cdot \mathbf{n}}{kT}\right) \quad \text{on } \partial V \quad (25)$$

2.5. Mechanical Problem

Without volume forces and acceleration forces, the balance of momentum at the continuum level is given by

$$\nabla \cdot \boldsymbol{\sigma} = 0 \quad (26)$$

It is completed by the BC $\boldsymbol{\sigma} \cdot \mathbf{n} = \mathbf{f}$, where \mathbf{f} is the prescribed traction on ∂V , and Hookes law

$$\boldsymbol{\sigma} = \mathbf{C} : (\boldsymbol{\epsilon} - \boldsymbol{\epsilon}^{in}) \quad (27)$$

for the total strain $\boldsymbol{\epsilon} = \frac{1}{2}(\nabla \mathbf{u} + \nabla \mathbf{u}^T)$ and the stiffness tensor \mathbf{C} .

3. Identification of the Back-Stresses

3.1. Free Energy

In addition to the external stress, an additional contribution to the mechanical force on dislocations arising from short-range interactions between dislocations must be considered. The corresponding back-stresses that must be subtracted from the external stress can be identified from statistical considerations^[15,23] or from energy-based approaches.^[24,25] As statistical approaches are not available for multiple slip and climb, we resort here to the second type of approach. The back-stresses and the resulting forces on the dislocations are identified from the dissipation inequality. For the total free energy, the following form is assumed

$$\Psi = \iiint_V (\psi^{el} + \psi^{in} + \psi^{chem}) dV + \iint_S \psi^{surf} dS \quad (28)$$

where $\psi^{el} = \psi^{el}(\boldsymbol{\epsilon}^{el}) = \frac{1}{2} \boldsymbol{\epsilon}^{el} : \mathbf{C} : \boldsymbol{\epsilon}^{el}$ is the elastic energy, ψ^{in} the microscopically stored elastic energy by the dislocation structures, $\psi^{chem} = \psi^{chem}(c_v)$ the chemical energy, and ψ^{surf} the surface energy of the LABs due to the dislocation networks. After the study by Wulfinghoff et al.,^[25] a regularized free energy function of the dislocation density tensor $\boldsymbol{\alpha}$

$$\psi^{in}(\boldsymbol{\alpha}) = \begin{cases} a\mu b \|\boldsymbol{\alpha}\| \ln\left(\frac{\|\boldsymbol{\alpha}\|}{\alpha_0}\right) + \frac{a\mu b}{2} \alpha_0 & \text{if } \|\boldsymbol{\alpha}\| > \alpha_0 \\ \frac{a\mu b}{2\alpha_0} \|\boldsymbol{\alpha}\|^2 & \text{else} \end{cases} \quad (29)$$

is assumed, where a is a numerical parameter, μ the shear modulus, and α_0 the regularization factor. According to Equation (12), the dislocation induced free energy is merely a function of the GNDs at the slip system level, that is, $\psi^{in}(\boldsymbol{\alpha}) \equiv \psi^{in}(\boldsymbol{\kappa}^g)$.

3.2. Application of the Dissipation Inequality

For simplicity, the derivation will not be carried out in the most general context but restricted to the assumptions made in the following simulations. Specifically, these assumptions and simplifications are as follows. 1. The dislocation content of the LABs is not affected by the dislocation nucleation process considered in Section 5 or by other dislocation interactions with the LABs for symmetry reasons. Whenever a dislocation moves toward the LABs, on the other side, a dislocation with opposite Burgers vector moves at the same velocity toward the LAB and both annihilate at the LAB as pictured in **Figure 4**. In accordance, the LABs constitute perfect sinks for dislocations similar to free surfaces. Furthermore, the surface contribution to the free energy ψ^{surf} remains constant and its time derivative vanishes. 2. The material velocity at the continuum level \mathbf{v} is assumed to be smooth everywhere, including across the LABs (in contrast to the dislocation velocities). 3. The LABs are perfect sinks for vacancies, similar to free surfaces. Physically, this means that vacancies are transported very fast along the LABs without altering the energy state of the LABs.

Following another study,^[19] the dissipation (free-energy imbalance) due to the dislocation motion and vacancy diffusion is

$$\mathcal{P}^{\text{Diss}} = \mathcal{P}^{\text{W}} + \mathcal{P}^{\text{Flow}} - \dot{\Psi} \geq 0 \quad (30)$$

where \mathcal{P}^{W} is the power of the external forces, which is given by

$$\mathcal{P}^{\text{W}} = \iint_{\partial V} \mathbf{f} \cdot \mathbf{v} \, dV \quad (31)$$

and $\mathcal{P}^{\text{Flow}}$ is the energy flow due to vacancy diffusion and dislocation transport. This energy flow is characterized by the potential μ_v for vacancy diffusion, respectively, and μ_d^{gs} for dislocation transport. Let \mathbf{n} denote the outward unit normal of the boundary of the solid V . Having in mind the assumptions made above, $\mathcal{P}^{\text{Flow}}$ must 0 surface ∂V as well as at the LABs, thus

$$\begin{aligned} \mathcal{P}^{\text{Flow}} = & - \iint_{\partial V} \mu_v \mathbf{J}_v \cdot \mathbf{n} \, dS - \sum_I \iint_{\text{LAB } I} \mu_v \mathbf{J}_v \cdot \mathbf{n} \, dS \\ & - \sum_{g,s} \iint_{\partial V} \mu_d^{\text{gs}} \mathbf{J}_d^{\text{gs}} \cdot \mathbf{n} \, dS - \sum_I \sum_{g,s} \iint_{\text{LAB } I} \mu_d^{\text{gs}} \mathbf{J}_d^{\text{gs}} \cdot \mathbf{n} \, dS \end{aligned} \quad (32)$$

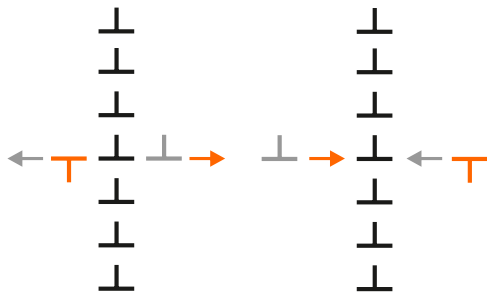


Figure 4. A symmetric LAB acting as a source or a sink.

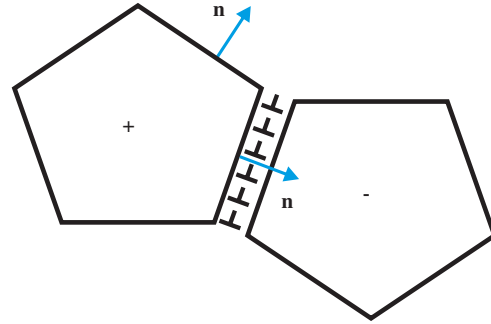


Figure 5. Convention for the outward normal \mathbf{n} at LAB delimiting two subgrains.

In the preceding equation, the brackets $[[x]]$ denote the jump of the quantity x across a LAB and a summation is made on the individual portions I of the LABs bounding two adjacent subgrains (see **Figure 5**). The normal vector \mathbf{n} of the LAB I points outward the “+” subgrain.

Applying the Gauss theorem to the dissipation Equation (30) along with the Equations (28), (31), (32), taking into account the stress BC $\boldsymbol{\sigma} \cdot \mathbf{n} = \mathbf{f}$ on ∂V , the equilibrium Equation (26), the diffusion equation (20), the dislocation balance equation (19), and the definition of the dislocation flux, $\mathbf{J}_d^{\text{gs}} = \rho^{\text{gs}} \mathbf{v}^{\text{gs}}$, we can transform the dissipation into

$$\begin{aligned} \mathcal{P}^{\text{Diss}} = & \iiint_V \boldsymbol{\sigma} : \dot{\boldsymbol{\epsilon}}^{\text{in}} \, dV + \iiint_V \left(\boldsymbol{\sigma} - \frac{\partial \psi^{\text{el}}}{\partial \boldsymbol{\epsilon}^{\text{el}}} \right) : \dot{\boldsymbol{\epsilon}}^{\text{el}} \, dV \\ & - \iiint_V (\nabla \mu_v \cdot \mathbf{J}_v + \mu_v \text{tr}(\dot{\boldsymbol{\epsilon}}^{\text{in}})) \, dV \\ & + \iiint_V \left(\mu_v - \frac{\partial \psi^{\text{chem}}}{\partial c_v} \right) \dot{c}_v \, dV - \sum_{g,s} \iiint_V \nabla \mu_d^{\text{gs}} \\ & \cdot (\rho^{\text{gs}} \mathbf{v}^{\text{gs}}) \, dV + \sum_g \iiint_V \left(-\mu_d^{\text{g}+} + \frac{\partial \psi^{\text{in}}}{\partial \kappa^{\text{g}}} \right) \nabla \cdot (\rho^{\text{g}+} \mathbf{v}^{\text{g}+}) \\ & + \left(-\mu_d^{\text{g}-} - \frac{\partial \psi^{\text{in}}}{\partial \kappa^{\text{g}}} \right) \nabla \cdot (\rho^{\text{g}-} \mathbf{v}^{\text{g}-}) \, dV \end{aligned} \quad (33)$$

Following the classical Coleman–Noll argument that $\mathcal{P}^{\text{Diss}} \geq 0$ must hold for all constitutive processes, the relations

$$\begin{aligned} \boldsymbol{\sigma} = \frac{\partial \psi^{\text{el}}}{\partial \boldsymbol{\epsilon}^{\text{el}}}, \quad \mu_v = \frac{\partial \psi^{\text{chem}}}{\partial c_v}, \quad \mu_d^{\text{g}+} = \frac{\partial \psi^{\text{in}}}{\partial \kappa^{\text{g}}} = \mu_d^{\text{g}}, \\ \mu_d^{\text{g}-} = -\frac{\partial \psi^{\text{in}}}{\partial \kappa^{\text{g}}} = -\mu_d^{\text{g}} \end{aligned} \quad (34)$$

follow. In the first and the second remaining integrals of Equation (33), the inelastic strain rate is rewritten at the slip system level, taking into account Equations (7) and (10). After some rearrangements we finally obtain

$$\begin{aligned} \mathcal{P}^{\text{Diss}} = & \iiint_V \sum_g \left(\rho^{gs+} v_{gl}^{gs+} - \rho^{gs-} v_{gl}^{gs-} \right) \left(b \tau^g - \nabla \mu_d^g \cdot \mathbf{m}^g \right) dV \\ & + \iiint_V \sum_g \left(\rho^{gs+} v_{cl}^{gs+} - \rho^{gs-} v_{cl}^{gs-} \right) \\ & \times \left(-b \zeta^g - \nabla \mu_d^g \cdot \mathbf{n}^g + b \mu_v \right) dV - \iiint_V \mathbf{J}_v \cdot \nabla \mu_v dV \end{aligned} \quad (35)$$

3.3. Identification of the Thermodynamic Forces

The first terms in the second brackets of the two first volume integrals in Equation (35) respectively correspond to the glide and climb components of the Peach–Köhler force at the slip system level, as can be recognized from a comparison with Equation (10). Hence, the back-stresses can be identified to be

$$\tau_b^{gs} = \begin{cases} \frac{1}{b} \nabla \mu_d^g \cdot \mathbf{m}^g & \text{if } s = + \\ -\frac{1}{b} \nabla \mu_d^g \cdot \mathbf{m}^g & \text{if } s = - \end{cases} \quad (36)$$

for glide and

$$\zeta_b^{gs} = \begin{cases} \frac{1}{b} \nabla \mu_d^g \cdot \mathbf{n}^g & \text{if } s = + \\ -\frac{1}{b} \nabla \mu_d^g \cdot \mathbf{n}^g & \text{if } s = - \end{cases} \quad (37)$$

for climb. The last term $b \mu_v$ in the second bracket of the climb part of Equation (35) corresponds to the osmotic force (compared with Equation (65)). Accordingly, the total climb force is

$$F_{cl}^{gs} = F_{cl}^{\text{mech},gs} + F_{cl}^{\text{osm},gs} = \begin{cases} -b \zeta^g - \nabla \mu_d^g \cdot \mathbf{n}^g + b \mu_v & \text{if } s = + \\ b \zeta^g + \nabla \mu_d^g \cdot \mathbf{n}^g - b \mu_v & \text{if } s = - \end{cases} \quad (38)$$

while the total glide force is

$$F_{gl}^{gs} = F_{gl}^{\text{mech},gs} = \begin{cases} b \tau^g - \nabla \mu_d^g \cdot \mathbf{m}^g & \text{if } s = + \\ -b \tau^g + \nabla \mu_d^g \cdot \mathbf{m}^g & \text{if } s = - \end{cases} \quad (39)$$

Recalling Equation (21) for vacancy diffusion, and as the dislocation densities ρ^{gs} are always positive, the positivity of the dissipation (35) is ensured if we choose constitutive laws of the form

$$v_{gl}^{gs} = \frac{1}{B_{gl}^{\text{drag}}} F_{gl}^{gs} \quad (40)$$

$$v_{cl}^{gs} = \frac{1}{B_{cl}^{\text{drag}} + B_{cl}^v} F_{cl}^{gs} \quad (41)$$

provided that $B_{gl}^{\text{drag}} > 0$ and $B_{cl}^{\text{drag}} + B_{cl}^v > 0$. Note that in the following section, the constitutive laws Equations (40) and (41) are directly derived from physical assumptions concerning the mechanisms retarding dislocation motion at the HIP temperature, which allows for the identification of the constants B_{gl}^{drag} , B_{cl}^{drag} , and B_{cl}^v . Introducing Equation (12) of the dislocation density tensor in the free energy (Equation 29), the back-stresses

can be further concretized. It is interesting to consider the special case in which only one slip system is activated. The microscopic free energy (Equation 29) becomes

$$\psi^{\text{in}}(\boldsymbol{\alpha}) = \begin{cases} a \mu b^2 |\kappa^g| \ln \left(\frac{b |\kappa^g|}{\alpha_0} \right) + \frac{a \mu b}{2} \alpha_0 & \text{if } b |\kappa^g| > \alpha_0 \\ \frac{a \mu b}{2 \alpha_0} b^2 |\kappa^g|^2 & \text{else} \end{cases} \quad (42)$$

and the glide component of the back-stress becomes

$$\tau_b^g = a \mu b \frac{1}{|\kappa^g|} \nabla \kappa^g \cdot \mathbf{m}^g \quad (43)$$

in the nonregularized case. At very high temperature, statistically stored dislocations are expected to be annihilated very fast by climbing, so that $|\kappa^g| \approx \rho^g$ and $\tau_b^g \approx a \mu b \frac{1}{\rho^g} \nabla \kappa^g \cdot \mathbf{m}^g$. The back-stress can be identified with that obtained by Groma^[15] after a coarse-graining procedure if $a = \frac{1}{2\pi(1-\nu)}$. Hence, the Equations (36) and (37) generalize this result to multiple slip and climb.

4. Evaluation of the Dislocation Velocity

4.1. Diffusion Equation for a Cottrell Atmosphere

It is assumed that the dislocation mobility is controlled by dragging a cloud (Cottrell atmosphere) of large solute atoms (rhenium and tungsten) by diffusion. Indeed, with a combination of transmission electron microscopy, atom probe tomography, and phase-field modeling, it has been shown in the study by Wu et al.^[26] that Re segregates at dislocations and retard their motion. In addition, according to the study by Fleischmann,^[27] the creep resistance of the γ -matrix increases by a factor of 20 when increasing the Re content from 0 to about 3 at%. Then, the dislocation velocity \tilde{v}^d results from the equilibrium of the forces (per unit length) on the dislocation

$$\tilde{\mathbf{F}}^{\text{PK}} + \tilde{\mathbf{F}}^{\text{drag}} + \tilde{\mathbf{F}}^{\text{osm}} = \mathbf{0} \quad (44)$$

The drag force expresses the interaction of the moving dislocation with the solute atoms. It is generally assumed to be a linear form of the velocity, which can be written as $\tilde{\mathbf{F}}^{\text{drag}} = -\mathbf{B}^{\text{drag}} \cdot \tilde{\mathbf{v}}^d$, where \mathbf{B}^{drag} is the diagonal matrix

$$\mathbf{B}^{\text{drag}} = \begin{bmatrix} B_{gl}^{\text{drag}} & 0 \\ 0 & B_{cl}^{\text{drag}} \end{bmatrix} \quad (45)$$

The osmotic force $\tilde{\mathbf{F}}^{\text{osm}}$ accounts for the effect of local deviations of the vacancy concentration with the equilibrium concentration as a climb dislocation either consumes or generates vacancies. Its component in the glide direction vanishes. Taking into account the equilibrium Equation (44), the dislocation velocity can be expressed as

$$\tilde{\mathbf{v}}^d = (\mathbf{B}^{\text{drag}})^{-1} \cdot (\tilde{\mathbf{F}}^{\text{PK}} + \tilde{\mathbf{F}}^{\text{osm}}) \quad (46)$$

The problem of solute drag by diffusion has been investigated by several authors^[16,28–30] in the ideal case of a straight dislocation. As solutions for climb could not be found in the literature,

the diffusion problem of the solute atoms was reanalyzed by FE for glide and climb. The following presentation follows closely.^[30] The diffusion problem for the solute atoms I ($I = \text{Re}$ or W), with their respective atomic concentration \tilde{c}_I and volume Ω_I , is solved in a coordinate system moving with the dislocation of velocity \tilde{v}^d . To consequently emphasize the fact that the concentration of the solute atoms I is defined at the dislocation level, the notation \tilde{c}_I is used in this section. The diffusion flux of the elements I is

$$\tilde{\mathbf{J}}_I = -\frac{D_I \tilde{c}_I (1 - \tilde{c}_I)}{\Omega kT} \nabla W_I - \frac{D_I}{\Omega} \nabla \tilde{c}_I - \frac{\tilde{c}_I}{\Omega} \tilde{v}^d \quad (47)$$

where Ω is the atomic volume of the alloy, D_I the mutual diffusion coefficient of the element I , and W_I the variation of energy when a solvent atom is replaced by a solute atom I , that is

$$W_I = \frac{A_I \gamma}{x^2 + y^2} \quad (48)$$

In the last equation, the prefactor A_I , which is given by

$$A_I = \frac{\mu b (1 + \nu)}{3\pi (1 - \nu)} (\Omega_I - \Omega) \quad (49)$$

characterizes the elastic interaction between solute and solvent atoms due to their difference of size. The interaction potential in Equation (48) becomes singular when $\mathbf{r} \rightarrow 0$. Hence, a regularized version has been used

$$\overline{W}_I = \frac{A_I \gamma}{x^2 + y^2 + r_c^2} \quad (50)$$

where $r_c \approx b$. Following the study by Sakamoto et al.,^[30] the value $r_c = 2b/3$ has been taken. The steady state is assumed and the conservation of species I reads

$$\nabla \cdot \tilde{\mathbf{J}}_I = 0 \quad (51)$$

which, together with the simplification $\tilde{c}_I \ll 1$, leads to

$$\Delta \tilde{c}_I + \nabla \cdot \left(\frac{\tilde{c}_I}{kT} \nabla W_I + \frac{\tilde{c}_I}{D_I} \tilde{v}^d \right) = 0 \quad (52)$$

in the plane perpendicular to the dislocation. The boundary value problem (BVP) is completed by the boundary condition $\tilde{c}_I(\infty) = c_{I,0}$, where $c_{I,0}$ is either the atomic concentration of Re or W at equilibrium. Once the Equation (52) has been solved for \tilde{c}_I , the dragging force per unit length on the dislocation due to the solute element I is found by integrating the force $\ast \nabla W$ exerted by a solute atom weighed by the volume concentration $\frac{\tilde{c}_I}{\Omega}$ on the whole domain, that is

$$\tilde{\mathbf{F}}_I^{\text{drag}} = \frac{1}{\Omega} \iint \tilde{c}_I \nabla W \, dS \quad (53)$$

Note that if the dislocation velocity vanishes, the equilibrium concentration distribution of the solute I around the dislocation is given by

$$c_{I,\text{eq}} = c_{I,0} \exp\left(-\frac{W_I}{kT}\right) \quad (54)$$

In accordance, the force $\tilde{\mathbf{F}}_I^{\text{drag}}$ can as well be evaluated by

$$\tilde{\mathbf{F}}_I^{\text{drag}} = \frac{1}{\Omega} \iint (\tilde{c}_I - c_{I,\text{eq}}) \nabla W \, dS \quad (55)$$

as the force exerted by the equilibrium distribution on the dislocation vanishes. In practice, the BVP (Equation 52) has been solved on a disk of radius $r_{\text{ext}} \gg b$, with the boundary condition $\tilde{c}_I(r_{\text{ext}}) = c_{I,0}$, and $\tilde{\mathbf{F}}_I^{\text{drag}}$ has been computed by Equation (55) to compensate for the finiteness of the disk. According to the literature,^[16,28–30] the drag force increases with the dislocation velocity until a maximum is reached at the critical value $v_{cI} \approx \frac{D_I kT}{A_I}$.

4.2. Glide Velocity

There is no osmotic force in the case of pure dislocation glide and the dislocation velocity follows from the component of Equation (44) in the glide direction \mathbf{m}^g

$$0 = \tilde{F}_{\text{gl}}^{\text{PK}} + \tilde{F}_{\text{gl}}^{\text{drag}} = \tilde{F}_{\text{gl}}^{\text{PK}} - B_{\text{gl}}^{\text{drag}} \tilde{v}_{\text{gl}}^d \quad (56)$$

At the (continuum) slip system level follows from Equation (56)

$$\tilde{v}_{\text{gl}}^{\text{gs}} = \frac{1}{B_{\text{gl}}^{\text{drag}}} F_{\text{gl}}^{\text{mech,gs}} \quad (57)$$

where $F_{\text{gl}}^{\text{mech,gs}}$ is given by Equation (39).

4.3. Climb Velocity

The derivation of the climb velocity follows closely the presentation in the study by Geers et al.^[21] and is briefly summarized for clarity. It is assumed that the jog concentration along the dislocation line is large enough so that the dislocation can be regarded as a perfect sink or source, which corresponds to the diffusion-limited regime identified by Balluffi.^[31] In accordance, vacancy equilibrium is satisfied along the dislocation, and climb is controlled by vacancy bulk diffusion.

A two-scale problem is considered: the (mesoscopic) continuum scale, which corresponds to the solution of Equation (23), and the (microscopic) dislocation scale, in which the vacancy concentration \tilde{c}_v is searched in a hollow cylinder around the core of a single dislocation. To simplify, the work done by the pressure when an atom is removed due to the volume change ΔV_r is neglected, which amounts to assuming that $\frac{1}{3} |\text{tr} \sigma \Delta V_r| \ll Q_v$. The diffusion potential simplifies to

$$\tilde{\mu}_v = \frac{kT}{\Omega} \left(\ln \frac{\tilde{c}_v}{1 - \tilde{c}_v} + \frac{Q_v}{kT} \right) \quad (58)$$

Introducing the equilibrium concentration of vacancies without dislocations c_{v0} given in Equation (24), the diffusion potential can be rewritten as

$$\bar{\mu}_v = \frac{kT}{\Omega} \ln\left(\frac{\tilde{c}_v}{c_{v0}}\right) \quad (59)$$

At the microscopic scale, when a dislocation climbs, vacancies are emitted or absorbed, depending on the climb direction (see **Figure 6**). If for example an excess of vacancies is available in the core region, an osmotic force appears, which drives the dislocation in the direction for which vacancies are consumed. Moreover, in accordance with the hypotheses made earlier, the local vacancy concentration around the core \tilde{c}_{vk} corresponds to the equilibrium concentration. The osmotic force at the dislocation level acts in the direction of the normal vector to the glide plane \mathbf{n}^g and is given by (see, e.g., the textbook by Hirth and Lothe^[16])

$$\bar{F}_{cl}^{osm} = -\frac{kT}{\Omega} (\mathbf{b} \cdot \boldsymbol{\zeta}) \ln\left(\frac{\tilde{c}_{vk}}{c_{v0}}\right) \quad (60)$$

bearing in mind the sign conventions introduced in Section 2.

The climb velocity and the vacancy flux around the dislocation core are related due to mass conservation. The relationship between the climb velocity and the vacancy concentrations in the dislocation core region \tilde{c}_{vk} and far away from the dislocation $\tilde{c}_{v\infty}$ has been obtained (see, e.g., the study by Bako et al.^[32]) by solving the stationary diffusion problem for a hollow cylinder of internal radius $r_c \approx b$ and external radius r_∞ and with the boundary conditions $c_v(r_c) = \tilde{c}_{vk}$ and $c_v(r_\infty) = \tilde{c}_{v\infty}$

$$\bar{v}_{cl}^d = \frac{2\pi D_v c_{v0}}{(\mathbf{b} \cdot \boldsymbol{\zeta}) \ln(r_\infty/r_c)} \left(\frac{\tilde{c}_{vk}}{c_{v0}} - \frac{\tilde{c}_{v\infty}}{c_{v0}}\right) \quad (61)$$

The external radius r_∞ is typically taken as a characteristic distance between dislocations. The equilibrium Equation (44) in the climb direction provides the second necessary condition.

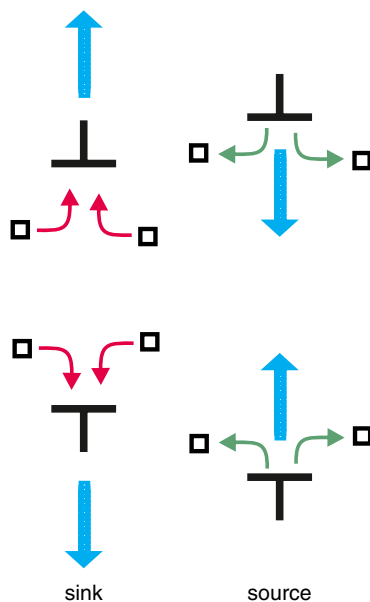


Figure 6. Climbing dislocation as a source or sink of vacancies.

$$0 = \bar{F}_{cl}^{PK} + \bar{F}_{cl}^{drag} + \bar{F}_{cl}^{osm} = \bar{F}_{cl}^{PK} - B_{cl}^{drag} \bar{v}_{cl}^d - \frac{kT}{\Omega} (\mathbf{b} \cdot \boldsymbol{\zeta}) \ln\left(\frac{\tilde{c}_{vk}}{c_{v0}}\right) \quad (62)$$

The set of Equations (61) and (62) is a nonlinear system that allows to determine \bar{v}_{cl}^d and \tilde{c}_{vk} . Assuming that $\frac{|\tilde{c}_{vk} - c_{v0}|}{c_{v0}} \ll 1$, it is advantageous to linearize Equation (62) to finally obtain

$$\begin{aligned} \bar{v}_{cl}^d &= \frac{1}{B_{cl}^{drag} + B_{cl}^v} \left(\bar{F}_{cl}^{PK} - \frac{kT}{\Omega} (\mathbf{b} \cdot \boldsymbol{\zeta}) \left(\frac{\tilde{c}_{v\infty}}{c_{v0}} - 1\right) \right) \\ &\approx \frac{1}{B_{cl}^{drag} + B_{cl}^v} (\bar{F}_{cl}^{PK} + \bar{F}_{cl}^{osm}) \end{aligned} \quad (63)$$

where the drag coefficient due to retardation by vacancy diffusion is defined as

$$B_{cl}^v = \frac{b^2 kT \ln(r_\infty/r_c)}{2\pi D_v c_{v0} \Omega} \quad (64)$$

Following the study by Geers et al.,^[21] the vacancy density far away from the dislocation $\tilde{c}_{v\infty}$ is identified with the vacancy density at the (mesoscopic) continuum level, that is, $c_v \approx \tilde{c}_{v\infty}$, which is obtained by solving the diffusion equation, Equation (23). Turning now to the continuum slip system level, we can infer from Equation (63) the dislocation climb velocities for each slip system

$$\begin{aligned} v_{cl}^{g+} &= \frac{1}{B_{cl}^{drag} + B_{cl}^v} \left(F_{cl}^{mech,g+} + \frac{kT}{\Omega} b \ln\left(\frac{c_v}{c_{v0}}\right) \right) \\ &= \frac{1}{B_{cl}^{drag} + B_{cl}^v} (F_{cl}^{mech,g+} + b\mu_v) \end{aligned} \quad (65)$$

$$\begin{aligned} v_{cl}^{g-} &= \frac{1}{B_{cl}^{drag} + B_{cl}^v} \left(F_{cl}^{mech,g-} - \frac{kT}{\Omega} b \ln\left(\frac{c_v}{c_{v0}}\right) \right) \\ &= \frac{1}{B_{cl}^{drag} + B_{cl}^v} (F_{cl}^{mech,g-} - b\mu_v) \end{aligned} \quad (66)$$

Note that for all slip systems, the dislocation velocity at the continuum level can finally be expressed in the compact form

$$\mathbf{v}^{gs} = \mathbf{M} \cdot (\mathbf{F}^{PK,gs} + \mathbf{F}^{b,gs} + \mathbf{F}^{osm,gs}) \quad (67)$$

where the mobility matrix \mathbf{M} is given by

$$\mathbf{M} = \begin{bmatrix} \frac{1}{B_{gl}^{drag}} & 0 \\ 0 & \frac{1}{B_{cl}^{drag} + B_{cl}^v} \end{bmatrix} \quad (68)$$

in the axes of the slip system g , which according to Equation (40) and (41) ensures dissipation positivity.

4.4. Solution of the Diffusion Problem by FE

The BVP (Equation 52) has been solved by FE with a mesh made of triangular quadratic elements. The external radius has been

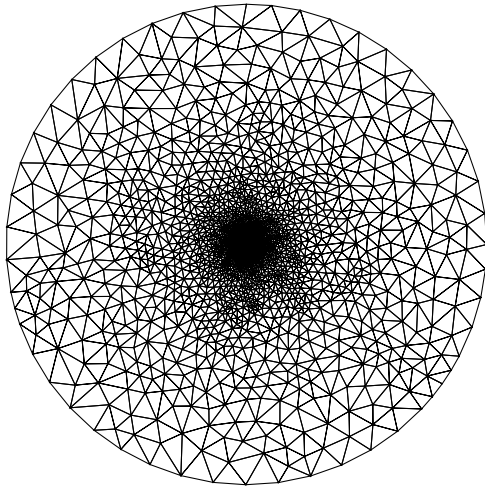


Figure 7. FE mesh for the resolution of the diffusion equation, Equation (52).

taken as $r_{\text{ext}} = 10^3 b$. The FE mesh is focused at the dislocation core, as can be seen in **Figure 7**.

The drag force exerted by either Re or W solute atoms has been calculated with the material constants provided in the Appendix 1 for several given glide velocities. The results are plotted in **Figure 8**. As expected, a quasilinear regime is observed until the velocity v_{cl} is reached, after which the drag force drops. Furthermore, the FE results are in good agreement with the quasianalytical solution derived by Fuentes-Samaniego et al.^[29] for $v \ll v_{\text{cl}}$. In the linear regime, the drag coefficients are found to obey a law of the form

$$B_{\text{gl}}^{\text{drag}} = \alpha^{\text{drag}} \frac{c_{\text{I},0} A_{\text{I}}^2}{\Omega D_{\text{I}} k T}, \quad (69)$$

where α^{drag} is a numerical factor. The value $\alpha^{\text{drag}} = 3$ has been found to reasonably approximate the quasilinear regime for both W and Re, as can be seen in **Figure 8**, for the example of W.

The total drag force is the sum of the contribution of Re and W, $\tilde{F}^{\text{drag}} = \tilde{F}_{\text{W}}^{\text{drag}} + \tilde{F}_{\text{Re}}^{\text{drag}}$. For easier comparison with the applied stress levels, the total drag force $F_{\text{gl}}^{\text{drag}}$ per unit line is divided by the Burgers vector and is plotted in **Figure 9**. It can be seen

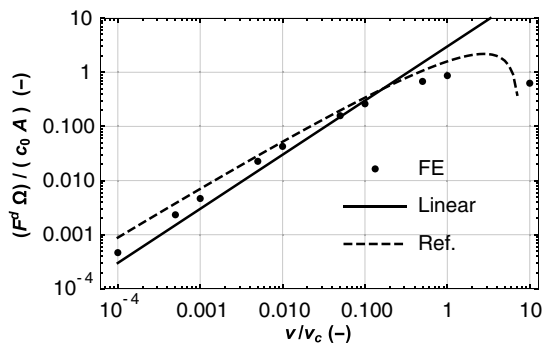


Figure 8. Normalized drag force due to dislocation glide computed by FE for W. Comparison with the linear model and with the solution obtained by Fuentes-Samaniego et al.^[29]

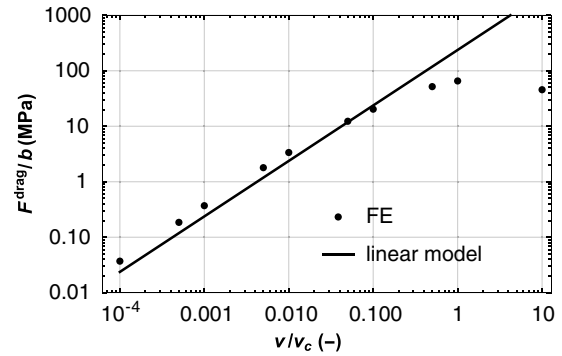


Figure 9. Total drag force per unit dislocation line scaled by the Burgers vector. Comparison with the linear model.

that the quasilinear regime applies up to an RSS level of about 10 MPa.

The total drag coefficient is then

$$B_{\text{gl}}^{\text{drag}} = \alpha^{\text{drag}} \frac{c_{\text{W},0} A_{\text{W}}^2}{\Omega D_{\text{W}} k T} + \alpha^{\text{drag}} \frac{c_{\text{Re},0} A_{\text{Re}}^2}{\Omega D_{\text{Re}} k T} \quad (70)$$

leading to the value $B_{\text{gl}}^{\text{drag}} = 3.7 \times 10^3 \text{ Nm}^{-2} \text{ s}$ at 1288 K.

The drag force opposing climb has been also computed and the results are presented for W in **Figure 10**. Higher resistance against climb than against glide can be observed. Accordingly, an increased drag coefficient $B_{\text{cl}}^{\text{drag}} = \beta_{\text{cl}} B_{\text{gl}}^{\text{drag}}$ with $\beta_{\text{cl}} = 3$ reasonably matching the FE results has been applied for climbing. Nevertheless, it should be acknowledged that the present calculation oversimplifies the problem at hand as for example the dislocation dissociation in partials (see, e.g., the study by Sills^[33]) is neglected. In the case of climb, this simplification is expected to result in a lower bound for the real drag force. Accordingly, this approach can only provide an estimate of the order of magnitude of the real drag coefficient.

The radius r_{∞} in Equation (64) is calculated by $r_{\infty} = \left(2\sqrt{\sum_{\text{gs}} \rho_{\text{gs}}^{\text{gs}}}\right)^{-1}$ with a maximum value equal to the sub-grain radius if the dislocation density is too small. With the parameters indicated in the appendix and with $r_{\infty} = 36 \mu\text{m}$, the drag coefficient for vacancy diffusion Equation (64) is found to be $B_{\text{cl}}^{\text{v}} \approx 5.1 \times 10^5 \text{ Nm}^{-2} \text{ s}$ with the lower bound for D_{v} and

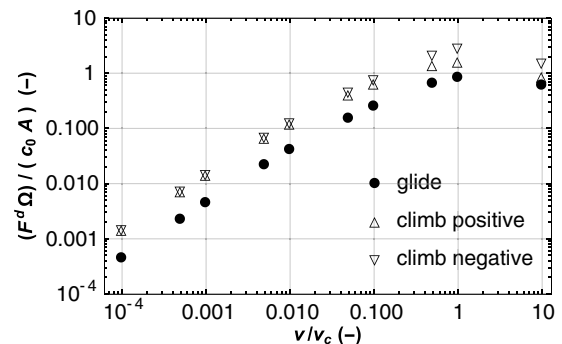


Figure 10. Normalized drag force due to dislocation glide and climb computed by FE for W.

$B_{cl}^v \approx 3.1 \times 10^3 \text{ Nm}^{-2} \text{ s}$ with the upper bound. In contrast, the aforementioned FE calculations suggest that $B_{cl}^{\text{drag}} \approx 10^4 \text{ Nm}^{-2} \text{ s}$ at 1288 K. It follows from these considerations that in the case of slow vacancy diffusion, dislocation climb is mainly controlled by vacancy diffusion and in the case of fast diffusion, both effects (vacancy diffusion and solute drag) are comparable.

5. LABs as Dislocation Sources

5.1. The Dislocation Flux at LABs

The nucleation of dislocations at grain boundaries has been experimentally observed^[34] and numerous attempts have been made to perform a mechanical analysis of the nucleation problem^[35–39] at either grain boundaries or LABs. The present model assumes that dislocations are nucleated at LABs (see **Figure 11**), which also act as obstacles to dislocation glide. After having reached the opposite LABs, the dislocations reorganize, thereby reducing their energy. This recovery process inside the LABs is believed to control the creep rate. However, there is no established model to describe this complex process. Hence, it has been decided to assume a stress-dependent nucleation rate $\nu_{\text{nuc}}(\tau^{gs})$ at the LABs and to fit it to the measured creep rates. However, the required quantity for the simulation is the dislocation flux vector $\mathbf{J}_{\text{nuc}}^{gs}$ at the LAB, for which it is further assumed that it only has a glide component J_{nuc}^{gs} in the direction of \mathbf{m}^g . If the LAB is perpendicular to the slip plane of the system (g, s) , the relationship

$$J_{\text{nuc}}^{gs} = \lambda^{gs} \nu_{\text{nuc}}^{gs} \quad (71)$$

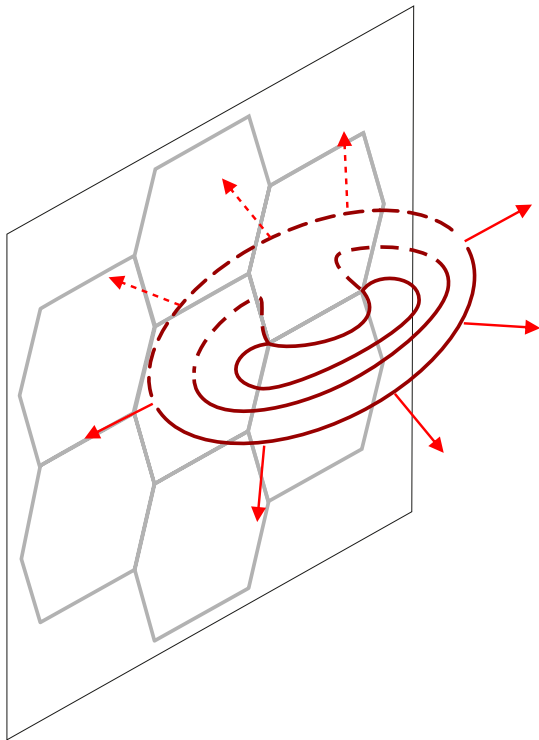


Figure 11. Frank–Read source in a LAB.

holds, where λ^{gs} is the surface density of the (g, s) sources in the LAB. In accordance with the previous considerations, $J_{\text{nuc}}^{gs} = J_{\text{nuc}}(\tau^{gs})$ is assumed to be a function of the local RSS τ^{gs} . The nucleation rate of a Frank–Read source $\nu_{\text{nuc}}(\tau^{gs})$ is controlled by the local dislocation glide velocity and has been estimated in other studies.^[40,41] Accordingly, if the glide velocity v_{gl}^{gs} is proportional to the shear stress τ^{gs} , then $\nu_{\text{nuc}}(\tau^{gs})$ must behave like τ^{gs} for large stresses. A flux function consistent with this property and Equation (71) is

$$J_{\text{nuc}}(\tau) = \tau \frac{a_1 \tau^{n_m}}{1 + a_2 \tau^{n_m}} \quad (72)$$

5.2. Relationship to the Creep Rate

If the creep rate is controlled by the nucleation rate at the LABs, the stationary creep rate can be estimated with some simplifications as follows. The dislocation flux $\rho^{gs} v_{\text{gl}}^{gs}$ must be divergence free according to Equation (16) if sources and sinks are absent. This flux must be exactly balanced by the inward flux at the LAB, that is, $J_{\text{nuc}}^{gs} = \rho^{gs} v_{\text{gl}}^{gs}$. From these considerations for the shear creep rate $\dot{\gamma}^{gs} = b J_{\text{nuc}}^{gs}$ and the overall creep rate in a solid specimen oriented along the $\langle 001 \rangle$ direction is

$$\dot{\epsilon}^{\text{in}} = 8f_{001} \dot{\gamma}^{gs} = 8f_{001} b J_{\text{nuc}}^{gs} \quad (73)$$

where f_{001} denotes the Schmid factor of the octahedral slip systems in a $\langle 001 \rangle$ specimen. The parameters of Equation (72) have been fit to the measured creep rates and are found to be $a_1 = 2.1 \times 10^{-39} \text{ Pa}^{-n_m-1} \text{ m}^{-1} \text{ s}^{-1}$, $a_2 = 6.6 \times 10^{-40} \text{ Pa}^{-n_m}$, and $n_m = 5.5$.

5.3. Boundary Condition for the Transport Equation and Model Calibration

The previous estimate needs to be adapted to the 2D model at hand. For this purpose, the creep tests have been simulated with a representative volume element (RVE) consisting of a circular 2D computational cell, as used for the pore shrinking simulations, however, without pores. The tensile axis is taken perpendicular to one slip plane, so that the two remaining slip systems are equally activated. Finally, a correction factor ϑ_{nuc} has been applied to Equation (72) and has been adjusted to the experimental creep rate.

The scalar dislocation flux required in the variational formulation of the balance Equation (16) is $\phi_{\text{nuc}}^{gs} = J_{\text{nuc}}^{gs} \cdot \mathbf{n}$, where \mathbf{n} is the outward normal vector of the LAB. At the locations of the LABs for which nucleation is active, that is, for which $(v^{gs} \cdot \mathbf{n} < 0)$, the prescribed dislocation flux is finally obtained as

$$\phi_{\text{nuc}}^{gs} = \vartheta_{\text{nuc}} J_{\text{nuc}}(\tau^{gs}) \mathbf{m}^g \cdot \mathbf{n} \quad (74)$$

where J_{nuc} is given by Equation (72).

With the previous boundary condition, the value of $\vartheta_{\text{nuc}} = 1.56$ has been found to achieve a reasonable agreement with the measured creep rates, as can be seen in **Figure 12**.

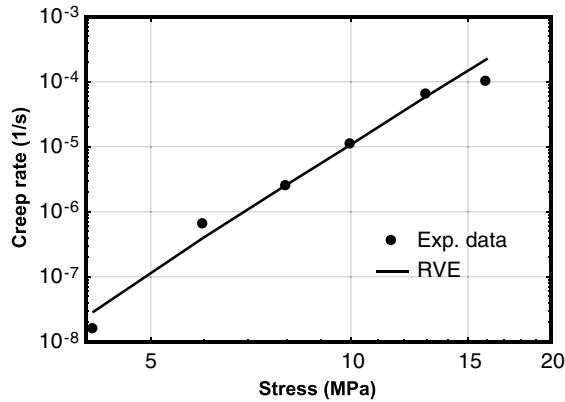


Figure 12. Creep rate of the uniaxial tensile creep tests. Experimental data and RVE simulations.

6. Simulations of Pore Shrinking

An outline of the simulation procedure is provided in Appendix 2. The simulations a priori depend on a number of parameters, like the pore size and its location with respect to the LAB or the value of the vacancy diffusion coefficient (see Appendix 1). In the following, the influence of these parameters is investigated by performing a number of comparative simulations of pore shrinking under HIP conditions for the alloy CMSX-4. The simulation parameters are summarized in Table 1.

6.1. Model of Pore in a Representative Volume (Surface) Element

Following other studies,^[3,11] a disk-shaped subgrain surrounded by LABs and containing a circular pore is taken as the representative computational cell (see Figure 13). The size of the subgrain has been determined from the synchrotron tomography data presented in the study by Epishin et al.^[3] A number of 2685 pores were counted in a volume of $5.4 \times 10^8 \mu\text{m}^3$, which corresponds to an average volume of $2.0 \times 10^5 \mu\text{m}^3$ per spherical cell and a

Table 1. Conditions of the pore shrinking simulations. Simulation no. 1e has been performed without dislocation nucleation (only vacancy diffusion).

Simulation No.	R_{pore} [μm]	Elasticity	D_v	Pore location	Pressure [MPa]
1a	4.7	Isotropic	D_v^{low}	Centered	103
1b	4.7	Cubic	D_v^{low}	Centered	103
1c	4.7	Cubic	D_v^{up}	Centered	103
1d	4.7	Cubic	D_v^{up}	Centered	150
1e	4.7	—	D_v^{up}	Centered	103
2a	9.4	Isotropic	D_v^{low}	Centered	103
2b	9.4	Isotropic	D_v^{up}	Centered	103
3	4.7	Isotropic	D_v^{low}	Noncentered	103

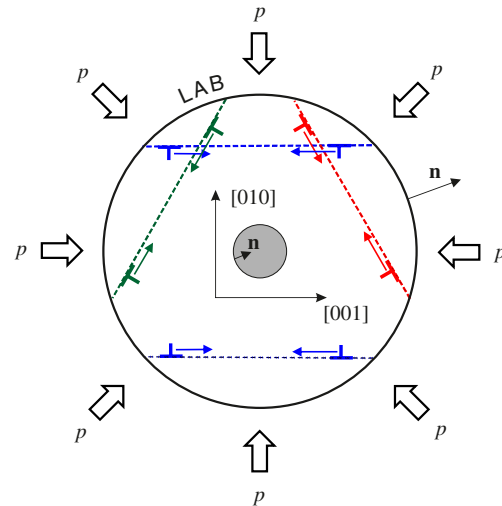


Figure 13. Arrangement of a pore in a circular subgrain surrounded by a LAB.

radius $R_{\text{LAB}} = 36 \text{ m}$. With the measured porosity of about 0.2%, this corresponds to a spherical pore of radius $R_{\text{pore},0} = 4.7 \text{ m}$. This value is also in agreement with the maximum of the pore size distribution reported in the study by Epishin et al.^[3]

The BC for vacancy diffusion is given by Equation (25). A pressure of $p = -\mathbf{n} \cdot \boldsymbol{\sigma} \cdot \mathbf{n} = 103 \text{ MPa}$ is continuously applied during a time interval of 100 s and then maintained on the external boundary, while the pore surface remains traction free. The more complex BC for dislocation transport are described in Sections 2.3 and 5.3.

A value for the factor α_0 that controls the regularization of the free energy (Equation (29)) has to be defined. The factor α_0 can be envisioned as a lower limit for the dislocation density, that is, below which a dislocation density ceases to be meaningful for the considered problem. Taking into account the previous dimensions, a dislocation density limit of $\rho_0 = 500 \mu\text{m}^{-2}$ has been taken, which corresponds to a mean distance between dislocations of about $1/\sqrt{\rho_0} = 0.04 \mu\text{m}$ and $\alpha_0 = b\rho_0 = 0.13 \mu\text{m}^{-1}$.

Let us denote $A_{\text{pore}} = \pi R_{\text{pore}}^2$ the pore area and $A_{\text{cell}} = \pi R_{\text{LAB}}^2$ the area of the computational cell. The interpretation of the simulation results requires the definition of a porosity decrease measure. Unfortunately, a straightforward comparison of the porosity with measurements is difficult as the ratio of the areas $A_{\text{pore}}/A_{\text{cell}}$ largely differs from the ratio of the corresponding volumes $R_{\text{pore}}^3/R_{\text{LAB}}^3$. To mitigate the effects of this discrepancy, the results are presented in terms of relative porosity referred to the initial area, which is defined as

$$\omega_{\text{pore}}(t) = \frac{A_{\text{pore}}(t)}{A_{\text{pore},0}} \quad (75)$$

The porosity decrease has two components: The first one is vacancy diffusion. Its contribution \dot{A}_{pore}^v is calculated by integrating the vacancy flux $\mathbf{J}_v \cdot \mathbf{n}$ around the pore surface^[11] and then

integrated during the simulation to obtain a variation $\Delta A_{\text{pore}}^{\text{v}} < 0$ of the pore area. The second one results from the inelastic deformations (dislocation creep). Its contribution is evaluated by calculating the deformation of the initially disk-shaped pore and its area change, $\Delta A_{\text{pore}}^{\text{in}} < 0$. Thereby, the pore area right after loading is taken as reference to account for elastic deformations. In summary, the pore area is updated during the simulation as $A_{\text{pore}} = A_{\text{pore},0} + \Delta A_{\text{pore}}^{\text{v}} + \Delta A_{\text{pore}}^{\text{in}}$.

6.2. Centered Pore

6.2.1. Small Pore

First, the case of a central pore of initial size $R_{\text{pore},0} = 4.7 \mu\text{m}$ is considered. A part of the simulations has been performed with cubic elasticity and with the constants indicated in the Appendix. The [001] axis is taken parallel to the horizontal slip plane (see Figure 13). Unfortunately, the introduction of crystal axes needed to define the elastic constants destroys the symmetry between the three slip systems. It is therefore interesting to consider also the isotropic case, for which the symmetry between the slip systems is maintained, and which is more comparable to the 3D case in this respect. The corresponding isotropic elastic constants have been estimated in the Appendix.

Figure 14 shows the distribution of the RSS in the hollow disk right after loading for isotropic elasticity. The RSS of the considered slip system vanishes on the symmetry lines. Figure 15 compares the RSS for isotropic and cubic elasticity on the path shown in Figure 14. The RSS are localized around the pore and are very low in the isotropic case on the external surface ($< 2 \text{ MPa}$), where the dislocation sources are located. With cubic elasticity, higher shear stresses up to 7.5 MPa are observed on the external boundary (LAB).

In the case of elastic isotropy (simulation No. 1a), Figure 16 shows the dislocation densities for one slip system and all six slip systems right after loading (100 s) and after 500 s. The dislocation densities remain extremely low (about 10^{-2} m^{-2}). This is due to the low RSS at the sources, which are hardly activated. However,

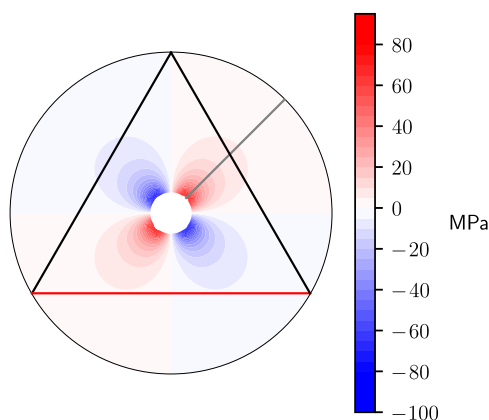


Figure 14. RSS distribution (in MPa) around a pore. Isotropic elasticity. The straight lines show the three glide planes. The red line is parallel to the glide plane of the considered system. The gray line represents the path for the plot in Figure 15.

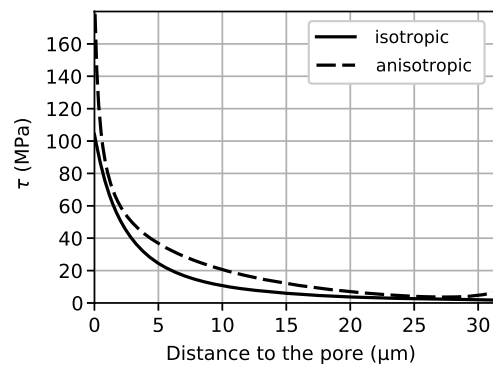


Figure 15. RSS (in MPa) on the path shown in Figure 14 and for the same slip system.

the dislocation motion qualitatively corresponds to the expected mechanism, which is schematically represented in Figure 17: dislocations are emitted at the LABs. They glide until they reach the symmetry line where the RSS vanishes. From there, they continue their motion by pure climb. Thereby, they consume vacancies emitted at the pore surface. Due to the low dislocation density, the pore mainly shrinks by vacancy diffusion in such a situation, as shown in Figure 18. However, the magnitude of the porosity reduction is much too low in comparison with the measurements.^[3]

If cubic elasticity is taken into account (simulation no. 1b), the higher RSS at the LAB leads to increased dislocation nucleation and thus a higher contribution of dislocation creep, as can be seen in Figure 19. Interestingly, the vacancy flux at the pore surface is also increased due to dislocation climb toward the pore, as schematically shown in Figure 17.

The previous simulations have been performed with the lower bound for the vacancy diffusion coefficient, that is, $D_v = D_v^{\text{low}}$ and the overall porosity decrease after 1 h remains very low. If the upper bound $D_v = D_v^{\text{up}}$ is assumed, Figure 20 shows that vacancy diffusion largely controls the porosity decrease, even in the case of cubic elasticity.

It should be mentioned that the measurements have shown that after 0.5 h the porosity is roughly halved.^[3] Figure 20 shows that a reasonable order of magnitude for the porosity decrease is obtained with the high value, $D_v = D_v^{\text{up}}$, of the vacancy diffusion coefficient for pure Ni. Figure 21 compares the HIP simulations with the small pore. For reference, the porosity decrease due to pure vacancy diffusion without dislocation creep (simulation no. 1e) is also represented. It is clear that the diffusion coefficient has the largest influence on porosity decrease. It is also interesting to see that dislocations significantly increase the porosity reduction rate with respect to pure vacancy diffusion.

Finally, a simulation (no. 1d) has been performed for a higher external pressure ($p = 150 \text{ MPa}$). As can be expected, a comparison of Figure 20 and 22 shows an increased contribution of dislocation creep with respect to the standard condition ($p = 103 \text{ MPa}$). It is worth mentioning that the assumption of pure vacancy diffusion leads to an approximately linear dependence of ΔA_{pore} on the external pressure. In contrast, the stress dependence of dislocation creep is superlinear, as results from the nucleation rate (72). Indeed, for better comparison, the

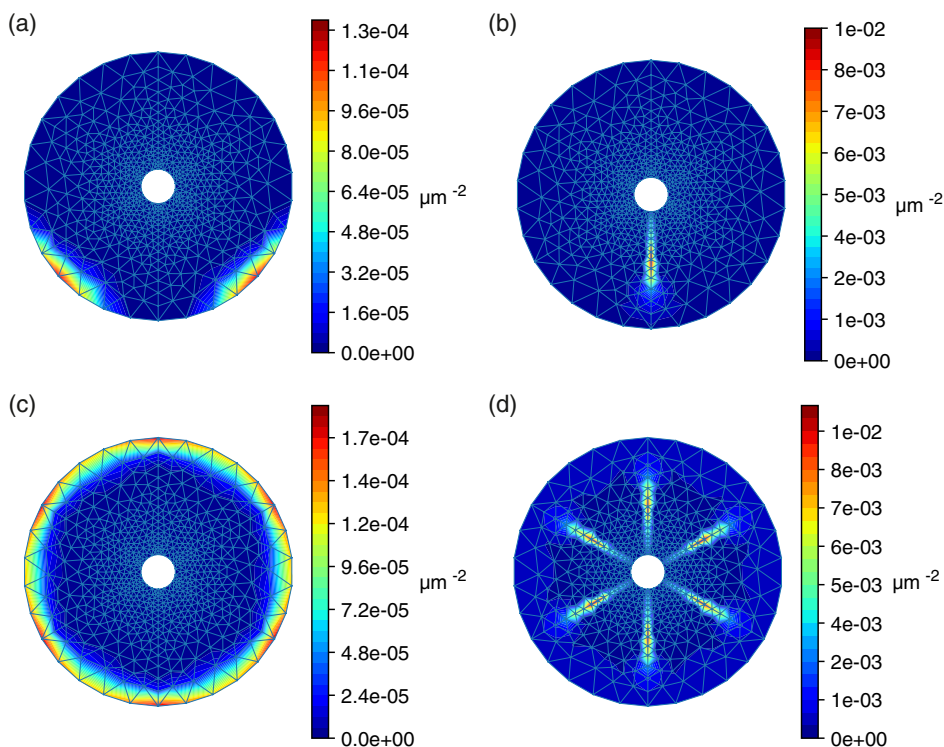


Figure 16. Dislocation density plots (in μm^{-2}) for simulation no. 1a. For one slip system (horizontal glide plane) after a) 100 and b) 500 s. For all slip systems after c) 100 and d) 500 s.

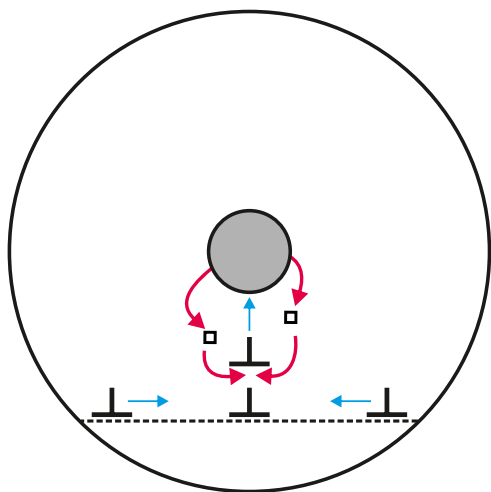


Figure 17. Schematic of the deformation process: dislocation gliding and then climbing toward the pore.

results of simulation no. 1c have been scaled by the factor 150/103 and represented in Figure 22. It can be verified that the porosity decrease calculated by the full model has a superlinear dependence on p . It is also recalled that the pure diffusion model underestimates the porosity reduction after 0.5 h for $p = 150 \text{ MPa}$.^[3] From these considerations, it can be concluded that the contribution of dislocation creep to porosity reduction becomes significant when the external pressure is increased.

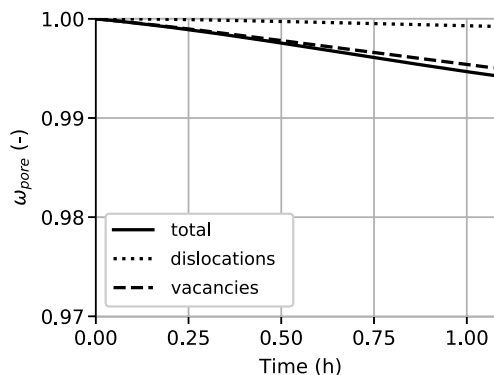


Figure 18. Relative decrease of the porosity. Centered small pore, isotropic elasticity, $D_v = D_v^{\text{low}}$. Simulation no. 1a.

6.2.2. Large Pore

The previous simulations have only exhibited a relatively low dislocation activity, mainly due to the low RSS at the LAB, leading to a low dislocation nucleation rate. To trigger a higher activity, the case of a large pore with radius $R_{\text{pore}} = 9.4 \mu\text{m}$ is considered in this section. Indeed, **Figure 23** shows that dislocation creep becomes the dominant mechanism for $D_v = D_v^{\text{low}}$.

For $D_v = D_v^{\text{up}}$, **Figure 24** shows that the contribution of vacancy diffusion is much higher than in the previous case as expected. However, it is also interesting to notice the significant contribution of dislocation creep and to compare it with the case

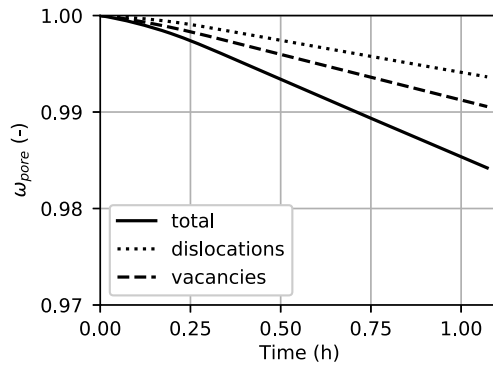


Figure 19. Relative decrease of the porosity. Centered small pore, cubic elasticity, $D_v = D_v^{low}$. Simulation no. 1b.

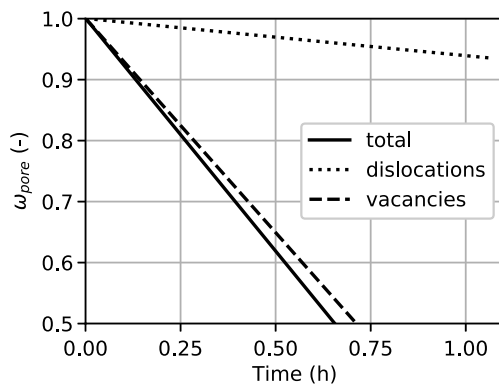


Figure 20. Relative decrease of the porosity. Centered small pore, cubic elasticity, $D_v = D_v^{up}$. Simulation no. 1c.

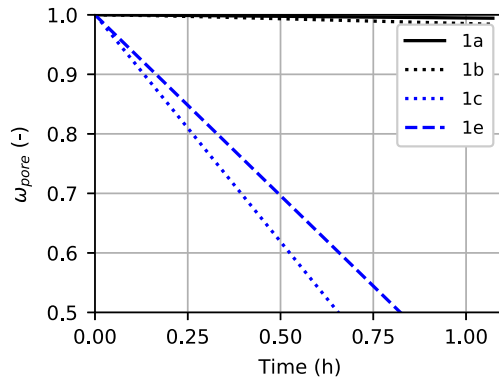


Figure 21. Relative decrease of the porosity. Centered small pore. The legend indicates the simulation number according to Table 1.

of the small pore in Figure 20. In contrast to the small pore situation, it is clear that dislocation creep can no longer be neglected. Here, it should be reminded that the experimental pore size histograms presented in the study by Epishin et al.^[3] showed that large pores (of diameter larger than 25 μm) already disappeared after 1 h HIP. In contrast, the predicted histogram (based on pure vacancy diffusion) still includes such large pores. The present results suggest that this discrepancy might be due to the contribution of dislocation creep that increases with the pore size.

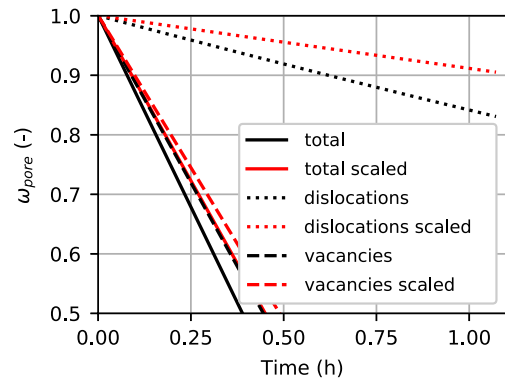


Figure 22. Relative decrease of the porosity. Centered small pore, cubic elasticity, $D_v = D_v^{up}$, $p = 150 \text{ MPa}$. Simulation no. 1d. Comparison with the results of simulation no. 1c scaled by 150/103.

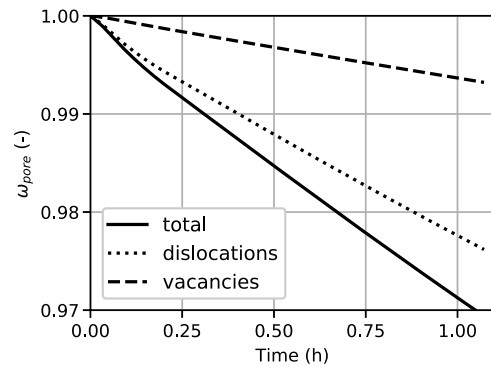


Figure 23. Relative decrease of the porosity. Centered large pore, isotropic elasticity, $D_v = D_v^{low}$. Simulation no. 2a.

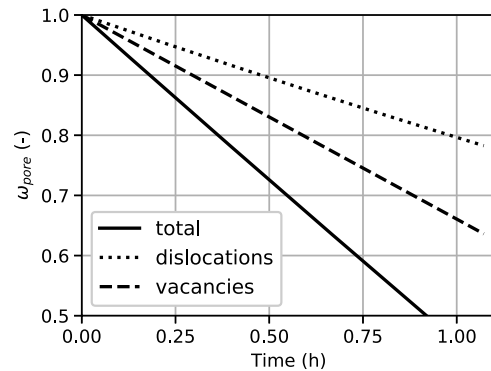


Figure 24. Relative decrease of the porosity. Centered large pore, isotropic elasticity, $D_v = D_v^{up}$. Simulation no. 2b.

6.3. Noncentered Small Pore

To demonstrate the importance of the position of the pore with respect to the LAB, the case of a pore located at coordinates $x = 18.2 \text{ m}$, $y = 0 \text{ m}$ is considered in this section. Usually, the pores are close to the LABs or interdendritic regions. The simulation results (no. 3) show that only two slip systems are activated,

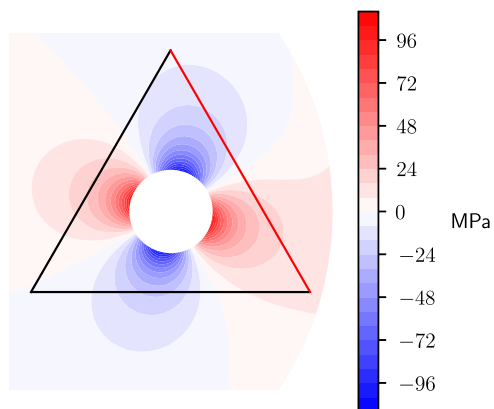


Figure 25. RSS distribution (in MPa) around a noncentered pore. The lines show the three glide planes. The red line is parallel to the glide plane of the considered system.

in contrast to the centered pore. **Figure 25** shows the RSS distribution for one of the most stressed slip systems. The comparison with **Figure 14** demonstrates that with a noncentered pore, higher shear stresses are locally attained on the LAB. In accordance, **Figure 26** shows that the local dislocation densities are much higher (locally up to 8 m^{-2}) than with the centered pore. Hence, a higher contribution of dislocation creep to pore shrinking is generally expected. Qualitatively, the motion is reminiscent of the previous case: the dislocations glide until they stop gliding and accumulate on a line where the sum of external and dislocation RSS vanishes and the motion continues by climb.

Indeed, the comparison of **Figure 27** with **Figure 18** shows that the closeness of the pore to the LAB enhances dislocation creep, whose contribution to pore shrinking becomes comparable with vacancy diffusion. In addition, the dislocations climbing toward the pore consume vacancies emitted at the pore surface (see **Figure 17**), which further accelerates pore shrinking. It should be mentioned that due to the highly localized character of the dislocation concentrations, a locally very fine mesh would be necessary to capture details of the dislocation distributions in these areas. Unfortunately, the numerical time step is dependent on the element size (see **Appendix 2**), which in practice hinders the use of a focused mesh in this region.

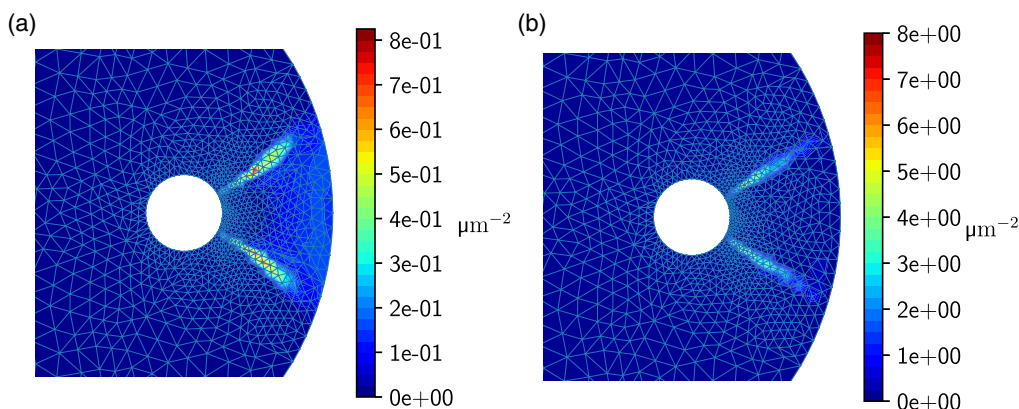


Figure 26. Dislocation density (in μm^{-2}) for all slip systems after a) 100 and b) 500 s (simulation No. 3).

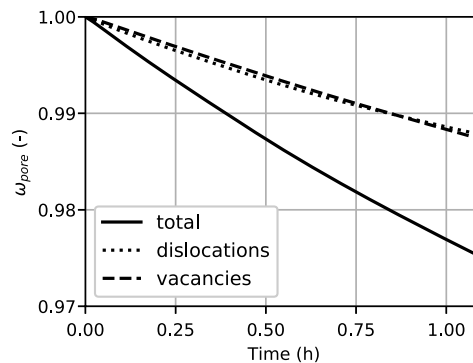


Figure 27. Relative decrease of the porosity. Noncentered small pore, isotropic elasticity, $D_v = D_v^{\text{ow}}$. Simulation no. 3.

6.4. Limitations of the Continuous Model

Theoretically, the mean distance between the dislocations should be small in comparison with the relevant geometrical dimensions to allow for a definition of dislocation density. In practice, this requirement cannot be satisfied in the present situation as at the beginning of the process, the subgrains are dislocation free. In fact, for the same reason, many applications of either local or strain-gradient CP at this scale in the literature are a priori questionable. Indeed the plasticity theory implicitly assumes that the use of plastic strains and hence of dislocation densities is meaningful at this scale. In particular, this issue was already raised in the study by Berdichevsky et al.^[42] Note that a conventional (2D) strain-gradient CP model is retrieved in the present model if the divergence term in Equation (16) is discarded.

To address this question in-depth, a comparison of the results with discrete dislocation (DD) simulations would be needed. For example, the comparisons of DD simulations of a crystalline material containing an elastic reinforcement with predictions of strain-gradient CP reported in the study by Bittencourt et al.^[43] show that a remarkable agreement can be obtained if the scaling parameters of the nonlocal terms are adequately adjusted. Unfortunately, the interactions between DDs and a pore are mathematically complex (see, e.g., the study by Li^[44] or Ruffini^[45]) and the authors are not aware of solutions for DDs that would enable a full DD simulation of the HIP process in conditions comparable with the present article.

In support of the present work, one can argue that in regions with very low dislocation densities, the disturbance of the stress field is negligible. The contribution to the free energy and the back-stresses also becomes minor as it corresponds to the regularized part, that is, the quadratic function of the dislocation density measure, of Equation (29). Hence, it can be reasonably assumed that the error resulting from the discreteness of dislocations in low-density areas is limited when looking at integral results, as the pore shrinking rate. In addition, simulations without back-stresses performed by the authors suggest that the influence of back-stresses, and thus of the short-range dislocation interactions, is limited in the present problem. However, it could be observed that the back-stress has a diffusive character and is thus greatly beneficial for the stability of the simulations.

7. Conclusion

A model for porosity annihilation in single-crystal nickel-base superalloys under HIP conditions has been developed. The model considers diffusion and dislocation creep around pores as the pore shrinking mechanisms. Due to the simplifications made, in particular, the two-dimensionality and the fact that the geometry is not updated, it is difficult to make quantitative comparisons with experimental measurements of porosity decrease during HIP like in other studies.^[3,6,7] However, the following conclusions can be made.

1) At the scale of the pores, it is mandatory to consider the heterogeneity of dislocation sources. In this work, it has been assumed that LABs are the only sources. The simulations of dislocation motion around the pore suggest that the location of the pore with respect to the dislocation sources plays a significant role: As the pore itself is the sole source of shear stresses, there is only little dislocation nucleation when the pore is sufficiently far away from the sources. In accordance, pore shrinking should be mostly controlled by vacancy diffusion. This could explain the overestimation of the pore shrinking rate by conventional CP as CP implicitly assumes that perfect dislocation sources are homogeneously distributed.

2) A large uncertainty exists regarding the value of the effective vacancy diffusion coefficient D_v . The porosity reduction predicted with the coefficient of pure Ni has the correct order of magnitude, in agreement with the results presented in the study by Epishin et al.^[3] In contrast, the simulations performed with the much lower value estimated for CMSX-4 in the study by Zhu et al.^[46] consistently underestimate the porosity reduction.

3) In the case of large pores and high external pressure (150 MPa), the simulations suggest that the contribution of dislocation creep is no longer negligible, which could explain the discrepancies of the pure diffusion model mentioned in the study by Epishin et al.^[3]

Appendix 1: Numerical Values of the Physical Parameters

This appendix presents the numerical values of the physical constants used for all calculations performed at the HIPing temperature, which is taken as $T = 1288$ °C.^[6]

Elastic Constants

The elastic constants of the alloy CMSX-4 were determined by the resonance method between room temperature (RT) and $T = 1300$ °C in the study by Epishin et al.,^[47] leading to the estimates $c_{11} = 185$ GPa, $c_{12} = 155$ GPa, and $c_{44} = 69$ GPa at $T = 1288$ °C.

As seen earlier, the classical treatment of solute drag by diffusion around a moving dislocation assumes isotropic elasticity. Unfortunately, there is no obvious choice of the appropriate equivalent isotropic constants to be used in this solution. The bulk modulus $\kappa_{\text{cubic}} = (c_{11} + c_{12})/3 = 165$ GPa is independent of the crystal orientation and is identical to that of a polycrystal. Hence, it is natural to keep its value for the equivalent isotropic constants, that is, $\kappa_{\text{cubic}} = \kappa_{\text{iso}}$. However, the shear modulus for a $\langle 001 \rangle$ plane is equal to c_{44} but is equal to $\frac{3c_{44}(c_{11}-c_{12})}{c_{11}-c_{12}+4c_{44}} = 20$ GPa for shear in a $\langle 111 \rangle$ plane. For definiteness, the isotropic shear modulus has been chosen in such a way that the prefactor K_{cubic} contained in the energy per line unit $\frac{W_{\text{cubic}}}{L} = \frac{K_{\text{cubic}}b^2}{4\pi} \log\left(\frac{R}{r_0}\right)$ of the straight-edge dislocation of the anisotropic material matches that of the energy per line unit $\frac{W_{\text{iso}}}{L} = \frac{\mu_{\text{iso}}b^2}{4\pi(1-\nu_{\text{iso}})} \log\left(\frac{R}{r_0}\right)$ of the isotropic solution, that is, $K_{\text{cubic}} = \frac{\mu_{\text{iso}}}{(1-\nu_{\text{iso}})}$. The expression of K_{cubic} as a function of the components of the stiffness (c_{11}, c_{12}, c_{44}) is given in the study by Hirth et al.^[16] After solving the resulting system of equations, the values $\mu_{\text{iso}} = 42$ GPa and $\nu_{\text{iso}} = 0.38$ are obtained. Note for comparison that these values are also close to the values $\mu_{\text{iso}} = 38$ GPa and $\nu_{\text{iso}} = 0.39$ found by averaging of the crystal constants after the Voigt–Reuss–Hill procedure for an isotropic polycrystal. In the following, the subscript iso will be omitted to simplify the notations.

Atomic Volumes

The atomic volumes at RT for Re and W have been taken to $\Omega_{\text{Re}} = 1.47 \times 10^{-29} \text{ m}^3$ and $\Omega_{\text{W}} = 1.57 \times 10^{-29} \text{ m}^3$.^[48] With the thermal dilatation coefficients provided in other studies,^[49] respectively,^[50] these atomic volumes take the values $\Omega_{\text{Re}} = 1.51 \times 10^{-29} \text{ m}^3$ and $\Omega_{\text{W}} = 1.60 \times 10^{-29} \text{ m}^3$ at the HIP temperature. The value of the atomic volume for the alloy CMSX-4 at RT has been deduced from the average lattice spacing $a_{\text{CMSX-4}} = 3.6 \times 10^{-10} \text{ m}$,^[51,52] leading to $\Omega_{\text{CMSX-4}} = \Omega = 1.16 \times 10^{-29} \text{ m}^3$ at RT and $\Omega_{\text{CMSX-4}} = \Omega = 1.24 \times 10^{-29} \text{ m}^3$ at the HIP temperature thermal dilatation coefficients provided in the study by Epishin et al.^[47] In accordance, the Burgers vector has the magnitude $\mathbf{b} = 2.6 \times 10^{-10} \text{ m}$ at $T = 1288$ °C.

Vacancies' Concentration

The atomic concentration of vacancies at equilibrium c_v^0 is given by (see, e.g., the study by Link et al.^[53])

$$c_v^0 = \exp\left(\frac{S_v^f}{R}\right) \exp\left(-\frac{H_v^f}{RT}\right) \quad (76)$$

where $S_v^f = 2.06 R$ and $H_v^f = 158.2 \text{ kJ mol}^{-1}$ are, respectively, the entropy and enthalpy vacancy formation in Ni and are taken from

the study by Link et al.^[53] From these values it follows that the atomic vacancy concentration at the HIPing temperature is $c_v^0 = 4 \times 10^{-5}$.

Diffusion Constants

According to the study by Violin et al.,^[54] the diffusion coefficient for vacancies D_v is related to the self-diffusion coefficient D_s by the relation

$$D_v = \frac{D_s}{\xi c_v^0} \quad (77)$$

where ξ is a correlation factor equal to 0.781 for face centered cubic (FCC) crystals. The coefficient for self-diffusion in nickel is given in the form^[55]

$$D_s = D_{s,0} \exp\left(-\frac{Q_s}{RT}\right) \quad (78)$$

where $D_{s,0} = 2.26 \times 10^{-4} \text{ m}^2 \text{ s}^{-1}$ and $Q_s = 287 \text{ kJ mol}^{-1}$. At the HIP temperature, $D_s = 5.63 \times 10^{-14} \text{ m}^2 \text{ s}^{-1}$ follows from Equation (78). This value is used in the study Epishin et al.^[3] and is close to the value $D_s = 5.34 \times 10^{-14} \text{ m}^2 \text{ s}^{-1}$ resulting from

the data presented in the study by Maier et al.^[56] However, it can be expected that the alloying elements considerably retard diffusion phenomena. Indeed, an effective coefficient D_s^{eff} that takes into account the alloying elements was derived for CMSX-4 in the study by Zhu et al.,^[46] which can be written as

$$D_s^{\text{eff}} = D_{s,0}^{\text{eff}} \exp\left(-\frac{Q^{\text{eff}}}{RT}\right) \quad (79)$$

where the effective activation energy Q^{eff} and the prefactor $D_{s,0}^{\text{eff}}$ are weighted averages of the contributions of the different solutes. For the activation energy, an arithmetic average leading to $Q^{\text{eff}} = 324.8 \text{ kJ mol}^{-1}$ is indicated. For the prefactor $D_{s,0}^{\text{eff}}$, an arithmetic average leads to $D_{s,0A}^{\text{eff}} = 1.29 \times 10^{-4} \text{ m}^2 \text{ s}^{-1}$ and $D_{s,0A}^{\text{eff}} = 1.75 \times 10^{-15} \text{ m}^2 \text{ s}^{-1}$ at the HIP temperature. However, the authors recommended the use of a harmonic mean for creep modeling, leading to the pre-factor $D_{s,0H}^{\text{eff}} = 2.56 \times 10^{-5} \text{ m}^2 \text{ s}^{-1}$ and $D_{s,H}^{\text{eff}} = 3.47 \times 10^{-16} \text{ m}^2 \text{ s}^{-1}$ at the HIP temperature. From what precedes, the values $D_s^{\text{up}} = 5.63 \times 10^{-14} \text{ m}^2 \text{ s}^{-1}$ and $D_s^{\text{low}} = 3.47 \times 10^{-16} \text{ m}^2 \text{ s}^{-1}$ can be respectively regarded as an upper and a lower bound for the effective self-diffusion coefficient of the CMSX-4 alloy. With these values, Equation (77)

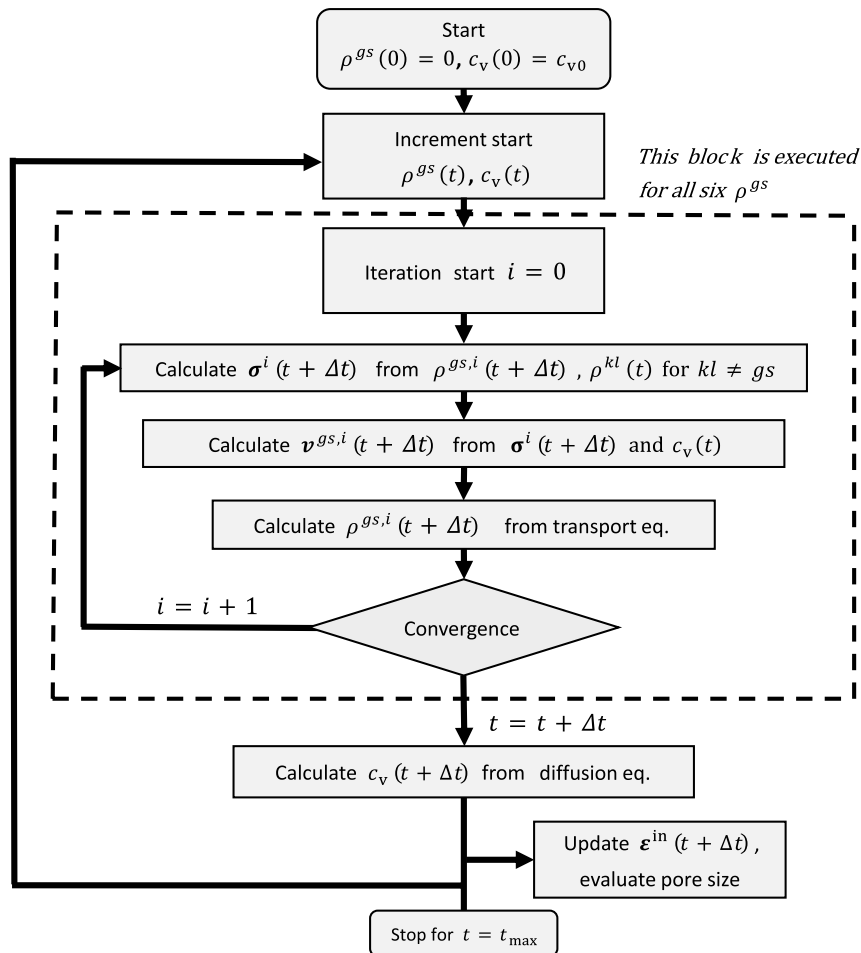


Figure 28. Flowchart of simulation.

provides the following bounds of the vacancy diffusion coefficient $D_v^{\text{up}} = 1.8 \times 10^{-9} \text{ m}^2 \text{ s}^{-1}$ and $D_v^{\text{low}} = 1.1 \times 10^{-11} \text{ m}^2 \text{ s}^{-1}$.

The interdiffusion coefficient for rhenium in nickel has been measured in the study by Epishin et al.^[57] and is given in the form

$$D_{\text{Re}} = D_{\text{Re},0} \exp\left(-\frac{Q_{\text{Re}}}{RT}\right) \quad (80)$$

where $D_{\text{Re},0} = 1.2 \times 10^{-4} \text{ m}^2 \text{ s}^{-1}$ and $Q_{\text{Re}} = 317 \text{ kJ mol}^{-1}$. At the HIP temperature, follows from Equation (80) $D_{\text{Re}} = 2.9 \times 10^{-15} \text{ m}^2 \text{ s}^{-1}$. The interdiffusion coefficient for tungsten in nickel has been measured in the study by Epishin et al.^[58] and is given in the form

$$D_{\text{W}} = D_{\text{W},0} \exp\left(-\frac{Q_{\text{W}}}{RT}\right) \quad (81)$$

where $D_{\text{W},0} = 2.5 \times 10^{-4} \text{ m}^2 \text{ s}^{-1}$ and $Q_{\text{W}} = 310 \text{ kJ mol}^{-1}$. At the HIP temperature, follows from Equation (81) $D_{\text{W}} = 1.1 \times 10^{-14} \text{ m}^2 \text{ s}^{-1}$.

The chemical composition of the alloy CMSX-4 is given, for example, in other studies.^[59,60] For the elements tungsten and rhenium, an atomic concentrations of $c_{\text{W}} = 0.02$, respectively, and $c_{\text{Re}} = 0.01$ are indicated.

Appendix 2: Numerical Solution of the Model Equations

The model equations have been solved by finite elements (FEs) with the open-source program FEniCS.^[61] Full details of the numerical methods will be provided in a projected paper.^[62] The resolution of transport equations is challenging. Indeed, the classical Galerkin methods or finite difference schemes lead to oscillating solutions but the usual procedures to alleviate these oscillations induce artificial diffusion. The flux-corrected transport method^[63–65] was developed to obtain an optimal compromise between spurious oscillations and diffusion. It is well suited for FE with nonstructured meshes. In particular, the positivity and conservation of the densities are guaranteed. This method has been implemented in FEniCS to take care of dislocation transport by glide and climb.

The application of the displacement-based Galerkin method to calculate the stresses has been found to lead to numerical instabilities, which are due to the fact that the stresses are not computed directly from the GND densities but rather from the plastic strains. To avoid these instabilities, it has been chosen to calculate the stresses directly from the GND densities, following a procedure proposed by Fressengeas.^[66]

Figure 28 shows the simulation sequence. The solutions of the eight partial differential equations (momentum balance, vacancy diffusion, and the six transport equations of the dislocations densities) are executed sequentially. Hence, the numerical coupling between those solutions is weak. A strong coupling might be possible but would require a considerable amount of implementation work. The time integration of the transport equations is semiimplicit: When solving the equations for the system (g, s) , the values of $\rho^{gs}(t + \Delta t)$ are updated but the values

$\rho^{kl}(t)$ for the other slip systems $(k, l) \neq (g, s)$ are taken at the start of the increment. The same applies for the vacancy concentration $c_v(t)$. Stability and convergence require sufficiently small time steps as usual for the numerical solution of transport equations: As a rule, the time increments must be smaller than the time needed by dislocations to cross an element and thus must be reduced with mesh refinement.

Supporting Information

Supporting Information is available from the Wiley Online Library or from the author.

Acknowledgements

This work was supported by the Deutsche Forschungsgemeinschaft (DFG, German Research Foundation) within the projects FE 933/2-1 and EP 136/1-1. The authors are grateful to Alphonse Finel, Yann Le Bouar, Antoine Ruffini (ONERA, France), Bernard Viguier, and Dominique Poquillon (CIRIMAT, France) for stimulating discussions. The authors are thankful to Georgia Künecke for improving the drawings and to Cetin Haftaoglu for technical assistance when performing the Finite Element simulations.

Open access funding enabled and organized by Projekt DEAL.

Conflict of Interest

The authors declare no conflict of interest.

Data Availability Statement

The data that support the findings of this study are available from the corresponding author upon reasonable request.

Keywords

creep, diffusion, dislocations, hot isostatic pressing, single-crystal superalloys

Received: September 30, 2021

Revised: December 1, 2021

Published online:

- [1] T. Link, S. Zabler, A. I. Epishin, A. Haibel, M. Bansal, X. Thibault, *Mater. Sci. Eng., A* **2006**, 425, 47.
- [2] X. Li, L. Wang, J. Dong, L. Lou, J. Zhang, *Metall. Mater. Trans. A* **2017**, 48, 2682.
- [3] A. I. Epishin, B. Camin, L. Hansen, M. Heuser, I. Lopez-Galilea, B. Ruttert, W. Theisen, B. Fedelich, *Adv. Eng. Mater.* **2021**, 23, 2100211.
- [4] A. I. Epishin, T. Link, H. Klingelhöffer, B. P. D. Portella, *Mater. High Temp.* **2010**, 27, 53.
- [5] K. Harris, G. L. Erickson, S. L. Sikkenga, W. D. Brentnall, J. M. Aurrecochea, K. G. Kubarych, *J. Mater. Eng. Perform.* **1993**, 2, 481.
- [6] A. I. Epishin, B. Fedelich, T. Link, T. Feldmann, I. L. Svetlov, *Mater. Sci. Eng., A* **2013**, 586, 342.
- [7] M. R. G. Prasad, S. Gao, N. Vajragupta, A. Hartmaier, *Crystals* **2020**, 10, 12.

- [8] M. R. G. Prasad, A. Neogi, N. Vajragupta, R. Janisch, A. Hartmaier, *Materials* **2021**, 14, 9.
- [9] A. I. Epishin, B. Fedelich, G. Nolze, S. Schrieffer, T. Feldmann, M. F. Ijaz, B. Viguier, D. Poquillon, Y. Le Bouar, A. Ruffini, A. Finel, *Metall. Mater. Trans. A* **2018**, 49, 3973.
- [10] A. I. Epishin, B. Fedelich, B. Viguier, S. Schrieffer, I. Svetlov, N. Petrushin, R. Saillard, A. Proietti, D. Poquillon, A. Chyrkin, *Mater. Sci. Eng.: A* **2021**, 825, 141880.
- [11] A. I. Epishin, B. S. Bokstein, I. L. Svetlov, B. Fedelich, T. Feldmann, Y. Le Bouar, A. Ruffini, A. Finel, B. Viguier, D. Poquillon, *Inorg. Mater. Appl. Res.* **2018**, 9, 57.
- [12] Y. V. Levinsky, *Rus. J. Non-Ferr. Met.* **2009**, 50, 298.
- [13] U. Brückner, A. I. Epishin, T. Link, *Acta Mater.* **1997**, 45, 5223.
- [14] T. Hochrainer, *J. Mech. Phys. Solids* **2016**, 88, 12.
- [15] I. Groma, F. Csikor, M. Zaiser, *Acta Mater.* **2003**, 51, 1271.
- [16] J. Hirth, J. Lothe, *Theory of Dislocations*, 2nd ed., John Wiley & Sons, New-York **1982**.
- [17] T. Mura, *Micromechanics of Defects in Solids*, Martinus Nijhoff Publishers, The Hague **1982**.
- [18] C. Teodosiu, *Elastic Models of Crystal Defects*, Springer-Verlag, Berlin Heidelberg **1982**.
- [19] M. Gurtin, E. Fried, L. Anand, *The Mechanics and Thermodynamics of Continua*, Cambridge University Press, Cambridge **2010**.
- [20] W. Blum, P. Eisenlohr, F. Breutinger, *Metall. Mater. Trans. A* **2002**, 33, 291.
- [21] M. G. D. Geers, M. Cottura, B. Appolaire, E. P. Busso, S. Forest, A. Villani, *J. Mech. Phys. Solids* **2014**, 70, 136.
- [22] Y. Gao, A. C. F. Cocks, *Acta Mech. Solida Sin.* **2009**, 22, 426.
- [23] P.-L. Valdenaire, Y. Le Bouar, B. Appolaire, A. Finel, *Phys. Rev. B* **2016**, 93, 214111.
- [24] N. Guenincault, S. Forest, *Acta Mech. Solida Sin.* **2013**, 29, 763.
- [25] S. Wulfinghoff, S. Forest, T. Böhlke, *J. Mech. Phys. Solids* **2015**, 79, 1.
- [26] X. Wu, S. K. Makineni, C. H. Liebscher, G. Dehm, J. Rezaei Mianroodi, P. Shanthraj, B. Svendsen, D. Bürger, G. Eggeler, D. Raabe, B. Gault, *Nat. Commun.* **2020**, 11, 389.
- [27] E. Fleischmann, C. Konrad, J. Preußner, R. Völkl, E. Affeldt, U. Glatzel, *Metall. Mater. Trans. A* **2015**, 46, 1125.
- [28] S. Takeuchi, A. S. Argon, *Philos. Mag. A* **1979**, 40, 65.
- [29] R. Fuentes-Samaniego, R. Gasca-Neri, J. P. Hirth, *Philos. Mag. A* **1984**, 49, 31.
- [30] M. Sakamoto, *Mater. Trans. JIM* **1989**, 30, 337.
- [31] R. W. Balluffi, *Phys. Status Solidi B* **1969**, 31, 443.
- [32] B. Bako, E. Clouet, L. M. Dupuy, M. Bletry, *Philos. Mag.* **2011**, 91, 3173.
- [33] R. B. Sills, W. Cai, *Philos. Mag.* **2016**, 96, 895.
- [34] L. E. Murr, *Metall. Trans. A* **1975**, 6, 505.
- [35] J. C. Li, *Trans. Metall. Soc. AIME.* **1963**, 227, 239.
- [36] R. Siems, R. Wagemann, *Phys. Status Solidi B* **1965**, 11, 731.
- [37] R. Varin, K. Kurzydowski, K. Tangri, *Mater. Sci. Eng., A* **1987**, 85, 115.
- [38] S. Kamat, J. Hirth, *Scr. Metall. Mater.* **1995**, 33, 1479.
- [39] L. Capolungo, M. Cherkaoui, J. Qu, *Int. J. Plast.* **2007**, 23, 561.
- [40] A. A. Benzerga, Y. Bréchet, A. Needleman, E. Van der Giessen, *Model. Simul. Mater. Sci.* **2003**, 12, 159.
- [41] P. K. Agnihotri, E. Van der Giessen, *Mech. Mater.* **2015**, 90, 37.
- [42] V. Berdichevsky, D. Dimiduk, *Scr. Mater.* **2005**, 52, 1017.
- [43] E. Bittencourt, A. Needleman, M. Gurtin, E. Van der Giessen, *J. Mech. Phys. Solids* **2003**, 51, 281.
- [44] Z. Li, Y. Li, J. Sun, X. Q. Feng, *J. Appl. Phys.* **2011**, 109, 113529.
- [45] A. Ruffini, Y. Le Bouar, A. Finel, *J. Mech. Phys. Solids* **2017**, 105, 95.
- [46] Z. Zhu, H. Basoalto, N. Warnken, R. Reed, *Acta Mater.* **2012**, 60, 4888.
- [47] A. I. Epishin, B. Fedelich, M. Finn, G. Künecke, B. Rehmer, G. Nolze, C. Leistner, N. Petrushin, I. Svetlov, *Crystals* **2021**, 11, 2.
- [48] C. N. Singman, *J. Chem. Educ.* **1984**, 61, 137.
- [49] J. B. Conway, *Properties of some refractory metals. Part III: Thermal expansion characteristics of Tungsten, Rhenium, Tantalum, Molybdenum, Niobium, W-25Re, Ta-10W, and Mo-50Re.*, Technical report Nr. GEMP-375 of the General Electric co., General Electric Co., Cincinnati, OH **1965**.
- [50] A. P. Müller, A. Cezairliyan, *Int. J. Thermophys.* **1990**, 11, 619.
- [51] R. Völkl, U. Glatzel, M. Feller-Kniepmeier, *Acta Mater.* **1998**, 46, 4395.
- [52] A. I. Epishin, U. Brückner, P. Portella, T. Link, *Scripta Mater.* **2003**, 48, 455.
- [53] T. Link, A. I. Epishin, M. Paulisch, T. May, *Mater. Sci. Eng., A* **2011**, 528, 6225.
- [54] T. E. Volin, R. W. Balluffi, *Phys. Status Solidi B* **1968**, 25, 163.
- [55] A. Engström, J. Ågren, *Z. Met.kd.* **1996**, 87, 92.
- [56] K. Maier, H. Mehrer, E. Lessmann, W. Schüle, *Phys. Status Solidi B* **1976**, 78, 689.
- [57] A. I. Epishin, A. O. Rodin, B. S. Bokshtein, G. Oder, T. Link, I. L. Svetlov, *Phys. Met. Metallogr.* **1984**, 116, 175.
- [58] A. I. Epishin, T. Link, G. Noltze, I. L. Svetlov, B. S. Bokshtein, A. O. Rodin, R. S. Neumann, G. Oder, *Phys. Met. Metallogr.* **2014**, 115, 21.
- [59] N. Wanderka, U. Glatzel, *Mater. Sci. Eng., A* **1995**, 203, 69.
- [60] D. Siebörger, H. Brehm, F. Wunderlich, U. Glatzel, D. Möller, *Z. Met.kd.* **2001**, 92, 58.
- [61] M. S. Alnæs, J. Blechta, J. Hake, A. Johansson, B. Kehlet, A. Logg, C. Richardson, J. Ring, M. E. Rognes, G. N. Wells, *Arch. Num. Soft.* **2015**, 3, 100.
- [62] T. Feldmann, B. Fedelich, A. Charmi, *Application of the Flux-Corrected Transport Method to Solve the Dislocation Transport Equations by Finite Elements*, **2021**, Unpublished.
- [63] D. Kuzmin, R. Lähner, S. Turek, *Flux-Corrected Transport: Principles, Algorithms, and Applications*, Scientific Computation, Springer Netherlands, Dordrecht **2012**.
- [64] D. Kuzmin, *J. Comput. Phys.* **2009**, 228, 2517.
- [65] D. Kuzmin, S. Turek, *J. Comput. Phys.* **2002**, 175, 525.
- [66] C. Fressengeas, *Mechanics of Dislocation Fields*, Wiley, Somerset **2017**.